

The Phase-I Trigger Readout Electronics Upgrade of the ATLAS Liquid Argon Calorimeters

G. Aad¹⁹, A.V. Akimov^{6, 22}, K. Al Khoury^{7a}, M. Aleksa⁶, T. Andeen³, C. Anelli³², N. Aranzabal⁶, C. Armijo², A. Bagulia²², J. Ban^{7a}, T. Barillari²³, F. Bellachia¹, M. Benoit⁵, F. Bernon¹⁹, A. Berthold⁹, H. Bervas²⁷, D. Besin²⁷, A. Betti⁸, Y. Bianga⁹, M. Biaut¹⁹, D. Boline²⁸, J. Boudreau²⁵, T. Bouedo¹, N. Braam³², M. Cano Bret¹⁴, G. Brooijmans^{7a}, H. Cai²⁵, C. Camincher^{6, 32}, A. Camplani^{13a, 34}, S. Cap¹, A. Carbone^{13a}, J.W.S. Carter³⁰, S.V. Chekulaev^{31a, 22}, H. Chen⁵, K. Chen⁵, N. Chevillot¹, M. Citterio^{13a}, B. Cleland^{25, *}, M. Constable^{31a}, S. de Jong³², A.M. Deiana⁸, M. Delmastro¹, B. Deng⁸, H. Deschamps²⁷, C. Diaconu¹⁹, A. Dik²², B. Dinkespiler¹⁹, N. Dumont Dayot¹, A. Emerman^{7a}, Y. Enari²⁹, P.J. Falke^{1, 33}, J. Farrell⁵, W. Fielitz⁵, E. Fortin¹⁹, J. Fragnaud¹, S. Franchino^{11a}, L. Gantel¹, K. Gigliotti², D. Gong⁸, A. Grabas²⁷, P. Grohs⁹, N. Guettouche¹⁹, T. Guillemin¹, D. Guo⁸, J. Guo^{10c}, L. Hasley⁸, C. Hayes^{28, 35}, R. Hentges⁹, L. Hervas⁶, M. Hils⁹, J. Hobbs²⁸, A. Hoffman⁵, D. Hoffmann¹⁹, P. Horn⁹, T. Hryn'ova¹, L. Iconomidou-Fayard¹², R. Iguchi²⁹, T. James⁸, J. Ye⁸, K. Johns², T. Junkermann^{11a}, C. Kahra¹⁸, E.F. Kay³², R. Keeler³², S. Ketabchi Haghighat³⁰, P. Kinget^{7b}, E. Knoops¹⁹, A. Kolbasin²², P. Krieger³⁰, J. Kuppambatti^{7b}, L.L. Kurchaninov^{31a}, E. Ladygin¹⁵, S. Lafrasse¹, M.P.J. Landon¹⁷, F. Lanni⁵, S. Latorre^{13a}, D. Laugier¹⁹, M. Lazzaroni^{13a, 13b}, X. Le⁸, P. Le Boulout²⁷, C.A. Lee⁵, M. Lefebvre³², M.A.L. Leite^{16c}, C. Leroy²¹, X. Li⁸, Z. Li^{19, 10b}, F. Liang⁸, H. Liu⁵, C. Liu⁸, T. Liu⁸, H. Ma⁵, L.L. Ma^{10b}, D.J. Mahon^{7a}, U. Mallik¹⁴, B. Mansoulie²⁷, A.L. Maslennikov^{24a, 24b}, N. Matsuzawa²⁹, R.A. McPherson^{32, a}, S. Menke²³, A. Milic^{30, 6}, Y. Minami²⁹, E. Molina²⁷, E. Monnier¹⁹, N. Morange¹², L. Morvaj^{6, 28}, J. Mueller²⁵, C. Mwewa⁵, R. Narayan⁸, N. Nikiforou^{3, 6}, I. Ochoa^{7a, 36a}, R. Oishi²⁹, D. Oliveira Damazio⁵, R.E. Owen²⁶, C. Pancake²⁸, D.K. Panchal³, G. Perrot¹, M.-A. Pleier⁵, P. Poffenberger^{32, *}, R. Porter³², S. Quan⁸, J. Rabel²⁵, A. Roy³, J.P. Rutherford², F. Sabatini^{13a}, F. Salomon¹⁹, E. Sauvan¹, A.C. Schaffer¹², R.D. Schamberger²⁸, Ph. Schwemling²⁷, C. Secord³², L. Selem¹, K. Sexton^{5, *}, E. Shafto²⁸, M.V. Silva Oliveira⁶, S. Simion¹², S. Singh³⁰, W. Sippach^{7a}, A.A. Snesarev²², S. Snyder⁵, M. Spalla²³, S. Stärz^{6, 20}, A. Straessner⁹, P. Strizenec^{4b}, R. Stroynowski⁸, V.V. Sulim²², J. Tanaka²⁹, S. Tang⁵, S. Tapprogge¹⁸, G.F. Tartarelli^{13a}, G. Tateno²⁹, K. Terashi²⁹, S. Tisserant¹⁹, D. Tompkins², G. Unal⁶, M. Unal³, K. Uno²⁹, A. Vallier^{6, 19}, S. Vieira de Souza¹⁸, R. Walker², Q. Wang^{7a}, C. Wang^{19, 10c}, R. Wang¹⁸, M. Wessels^{11a}, I. Wingerter-Seez¹, K. Wolniewicz⁵, W. Wu^{5, 10c}, Z. Xiandong⁸, R. Xu³, H. Xu⁵, S. Yamamoto²⁹, Y. Yang²⁹, H. Zaghia²⁷, J. Zang²⁹, T. Zhang²⁹, H.L. Zhu^{5, 10a}, V. Zhulanov^{24a, 24b}, E. Zonca^{27, *}, G. Zuk²⁵.

¹LAPP, Univ. Savoie Mont Blanc, CNRS/IN2P3, Annecy ; France.

²Department of Physics, University of Arizona, Tucson AZ; United States of America.

³Department of Physics, University of Texas at Austin, Austin TX; United States of America.

⁴(^a)Faculty of Mathematics, Physics and Informatics, Comenius University, Bratislava; (^b)Department of Subnuclear Physics, Institute of Experimental Physics of the Slovak Academy of Sciences, Kosice; Slovak Republic.

⁵Physics Department, Brookhaven National Laboratory, Upton NY; United States of America.

⁶CERN, Geneva; Switzerland.

⁷(^a)Nevis Laboratory, Columbia University, Irvington NY; (^b)Department of Electrical Engineering, Columbia University, New York NY; United States of America.

⁸Physics Department, Southern Methodist University, Dallas TX; United States of America.

⁹Institut für Kern- und Teilchenphysik, Technische Universität Dresden, Dresden; Germany.

- ¹⁰(^a) Department of Modern Physics and State Key Laboratory of Particle Detection and Electronics, University of Science and Technology of China, Hefei; (^b) Institute of Frontier and Interdisciplinary Science and Key Laboratory of Particle Physics and Particle Irradiation (MOE), Shandong University, Qingdao; (^c) School of Physics and Astronomy, Shanghai Jiao Tong University, Key Laboratory for Particle Astrophysics and Cosmology (MOE), SKLPPC, Shanghai; (^d) Tsung-Dao Lee Institute, Shanghai; China.
- ¹¹(^a) Kirchhoff-Institut für Physik, Ruprecht-Karls-Universität Heidelberg, Heidelberg; (^b) Physikalisches Institut, Ruprecht-Karls-Universität Heidelberg, Heidelberg; Germany.
- ¹²IJCLab, Université Paris-Saclay, CNRS/IN2P3, 91405, Orsay; France.
- ¹³(^a) INFN Sezione di Milano; (^b) Dipartimento di Fisica, Università di Milano, Milano; Italy.
- ¹⁴University of Iowa, Iowa City IA; United States of America.
- ¹⁵Joint Institute for Nuclear Research, Dubna; Russia.
- ¹⁶(^a) Departamento de Engenharia Elétrica, Universidade Federal de Juiz de Fora (UFJF), Juiz de Fora; (^b) Universidade Federal do Rio De Janeiro COPPE/EE/IF, Rio de Janeiro; (^c) Instituto de Física, Universidade de São Paulo, São Paulo; Brazil.
- ¹⁷School of Physics and Astronomy, Queen Mary University of London, London; United Kingdom.
- ¹⁸Institut für Physik, Universität Mainz, Mainz; Germany.
- ¹⁹CPPM, Aix-Marseille Université, CNRS/IN2P3, Marseille; France.
- ²⁰Department of Physics, McGill University, Montreal QC; Canada.
- ²¹Group of Particle Physics, University of Montreal, Montreal QC; Canada.
- ²²P.N. Lebedev Physical Institute of the Russian Academy of Sciences, Moscow; Russia.
- ²³Max-Planck-Institut für Physik (Werner-Heisenberg-Institut), München; Germany.
- ²⁴(^a) Budker Institute of Nuclear Physics and NSU, SB RAS, Novosibirsk; (^b) Novosibirsk State University Novosibirsk; Russia.
- ²⁵Department of Physics and Astronomy, University of Pittsburgh, Pittsburgh PA; United States of America.
- ²⁶Particle Physics Department, Rutherford Appleton Laboratory, Didcot; United Kingdom.
- ²⁷IRFU, CEA, Université Paris-Saclay, Gif-sur-Yvette; France.
- ²⁸Departments of Physics and Astronomy, Stony Brook University, Stony Brook NY; United States of America.
- ²⁹International Center for Elementary Particle Physics and Department of Physics, University of Tokyo, Tokyo; Japan.
- ³⁰Department of Physics, University of Toronto, Toronto ON; Canada.
- ³¹(^a) TRIUMF, Vancouver BC; (^b) Department of Physics and Astronomy, York University, Toronto ON; Canada.
- ³²Department of Physics and Astronomy, University of Victoria, Victoria BC; Canada.
- ³³Physikalisches Institut, Universität Bonn, Bonn; Germany.
- ³⁴Niels Bohr Institute, University of Copenhagen, Copenhagen; Denmark.
- ³⁵Department of Physics, University of Michigan, Ann Arbor MI; United States of America.
- ³⁶(^a) Laboratório de Instrumentação e Física Experimental de Partículas - LIP, Lisboa; (^b) Departamento de Física, Faculdade de Ciências, Universidade de Lisboa, Lisboa; (^c) Departamento de Física, Universidade de Coimbra, Coimbra; (^d) Centro de Física Nuclear da Universidade de Lisboa, Lisboa; (^e) Departamento de Física, Universidade do Minho, Braga; (^f) Departamento de Física Teórica y del Cosmos, Universidad de Granada, Granada (Spain); (^g) Dep Física and CEFITEC of Faculdade de Ciências e Tecnologia, Universidade Nova de Lisboa, Caparica; (^h) Instituto Superior Técnico, Universidade de Lisboa, Lisboa; Portugal.
- ^a Also at Institute of Particle Physics (IPP); Canada.

* Deceased

The Phase-I trigger readout electronics upgrade of the ATLAS Liquid Argon calorimeters enhances the physics reach of the experiment during the upcoming operation at increasing Large Hadron Collider luminosities. The new system, installed during the second Large Hadron Collider Long Shutdown, increases the trigger readout granularity by up to a factor of ten as well as its precision and range. Consequently, the background rejection at trigger level is improved through enhanced filtering algorithms utilizing the additional information for topological discrimination of electromagnetic and hadronic shower shapes. This paper presents the final designs of the new electronic elements, their custom electronic devices, the procedures used to validate their proper functioning, and the performance achieved during the commissioning of this system.

Reproduction of this article or parts of it is allowed as specified in the CC-BY-4.0 license.

Contents

1	Introduction	4
2	Overview of the LAr readout electronics	5
3	New Front-End electronics	9
3.1	Baseplanes	9
3.2	Layer Sum Boards	12
3.3	LAr Trigger Digitizer Boards	13
4	New Back-End electronics	25
4.1	LAr carrier	25
4.2	LAr trigger processing mezzanine	27
4.3	Intelligent platform management controller	29
4.4	Back-End firmware	30
5	Integration tests	40
5.1	Front-End boards integration tests	40
5.2	Back-End boards integration tests	41
5.3	Full chain tests	44
5.4	System latency	52
6	Conclusion	53

1 Introduction

During the second Large Hadron Collider (LHC) Long Shutdown (LS2), the Liquid Argon (LAr) calorimeters of the ATLAS experiment have been equipped with new trigger readout electronics [1], which provides digital information to the ATLAS trigger system [2]. The purpose of this so-called Phase-I upgrade is to enhance the physics reach of the experiment during the upcoming operation at increasing LHC luminosities. ATLAS ran in the Run 2 data taking period (years 2015–2018) at a typical maximum instantaneous luminosity of $1.9 \times 10^{34} \text{ cm}^{-2} \text{ s}^{-1}$ and with an average mean number of proton-proton interactions of $\langle \mu \rangle = 33$ [3]. During Run 3 (years 2022–2025) the instantaneous luminosity was originally expected to increase to a peak value of $3 \times 10^{34} \text{ cm}^{-2} \text{ s}^{-1}$, with $\langle \mu \rangle \approx 80$ [1]. The updated LHC plan for Run 3 targets a beam intensity increase of 50% compared to Run 2 with a luminosity leveled to $2 \times 10^{34} \text{ cm}^{-2} \text{ s}^{-1}$ over periods up to 12 hours. The center-of-mass energy will also be raised from $\sqrt{s} = 13 \text{ TeV}$ to 13.6 TeV . These changes will result in an overall detector occupancy increase, while the first level trigger (L1) bandwidth will remain at 100 kHz during Run 3. If the currently used LAr trigger readout system, referred to as *legacy* trigger readout in the following, were to remain unchanged, the transverse energy (E_T) trigger thresholds would need to be raised, degrading the physics performance. To avoid this efficiency loss and enhance the physics reach of the experiment in Run 3 and beyond, the new system installed during LS2 increases the readout granularity by up to a factor of ten: instead of summing the E_T of calorimeter cells in areas as small as $\Delta\eta \times \Delta\phi = 0.1 \times 0.1$ to form the so-called *Trigger Towers* of the legacy readout, additional lateral and longitudinal segmentation is introduced to form smaller clusters called *Super Cells*. Trigger Towers are typically split longitudinally into four layers, and some layers are split laterally

along η into four strips each. One Super Cell can thus cover an area as small as $\Delta\eta \times \Delta\phi = 0.025 \times 0.1$, depending on which longitudinal layer it is located in. In addition, the precision and range of the E_T measurement is also increased. Consequently, the background rejection at trigger level is improved due to better filtering algorithms being possible already at L1, based on topological discrimination between electromagnetic shower shapes and hadronic activity. In particular, the resulting electron, photon and tau lepton identification is more efficient. Furthermore, thanks to more advanced reconstruction algorithms and better pile-up subtraction techniques, the energy resolution for electromagnetic, jet and missing E_T objects is improved, leading to a sharper rise of the per-event trigger efficiency toward its plateau value.

The Phase-I upgrade project is part of a broad upgrade program of the LAr calorimeters through the lifetime of the LHC and is fully compatible with the future Phase-II upgrade program of the ATLAS experiment planned for the third Long Shutdown (LS3) in 2026–2028.

This paper presents the new system, initially proposed in Reference [1] and installed during LS2, together with its performance. The final designs of the new electronic boards and their Application-Specific Integrated Circuits (ASICs) are described as well as the procedures used to validate their proper functioning. The basic performance achieved during the commissioning of this system is also presented. In Section 2, the legacy readout electronics is briefly recapitulated and the new trigger readout electronics is introduced, as are the new data paths. The new electronics installed on the ATLAS detector (Front-End) and off the detector (Back-End) is described in Sections 3 and 4, respectively. Finally, the integration tests performed to validate the full chain of this new readout electronics are reported in Section 5 before the conclusions are presented in Section 6.

2 Overview of the LAr readout electronics

The readout electronics of the LAr calorimeters is designed to record energies approximately ranging from 50 MeV to 3 TeV, measured in 182418 calorimeter cells. The energy resolution of the calorimeter for electromagnetic showers can be written as $\sigma_E/E = a/\sqrt{E} \oplus b \oplus c/E$, with an intrinsic sampling term a that is typically 10–11% $\sqrt{\text{GeV}}$ [4, 5], a constant term b that is 1–2% [6], and a noise term c that is 10–600 MeV without pile-up contribution [7] and is expected to be 30 MeV–3 GeV in Run 3 pile-up conditions [1], depending on the pseudorapidity region considered (up to $|\eta| < 3.2$). The triangular pulse coming from the ionization in a LAr cell is shaped into a bipolar pulse that is sampled at 40 MHz. The digitized samples are read at the L1 trigger rate, that can go up to 100 kHz. The LAr calorimeter system is composed of four different components: the electromagnetic barrel (EMB) and end-caps (EMEC), both referred to as EM calorimeters; the hadronic end-cap (HEC); and the forward calorimeter (FCal). These components are divided in two sides, A and C, oriented respectively along the positive and negative z -axis of the experiment. The LAr readout electronics is divided into a Front-End and a Back-End system, both interconnected by cables and optical fibers as shown in Figure 1.

The Front-End system is composed of 58 Front-End Crates (FECs), each hosting at most two baseplanes which interconnect the following legacy system boards:

Front-End Boards (FEBs): process typically 128 channels, each in a specific longitudinal layer of the calorimeter. They amplify, shape, sample and digitize the ionization signals and transmit them to the Back-End readout. The analog sums needed for the trigger system are also prepared by the Linear Mixers and the Layer Sum Boards (LSBs), both hosted on the FEBs. The Linear Mixer electronics is

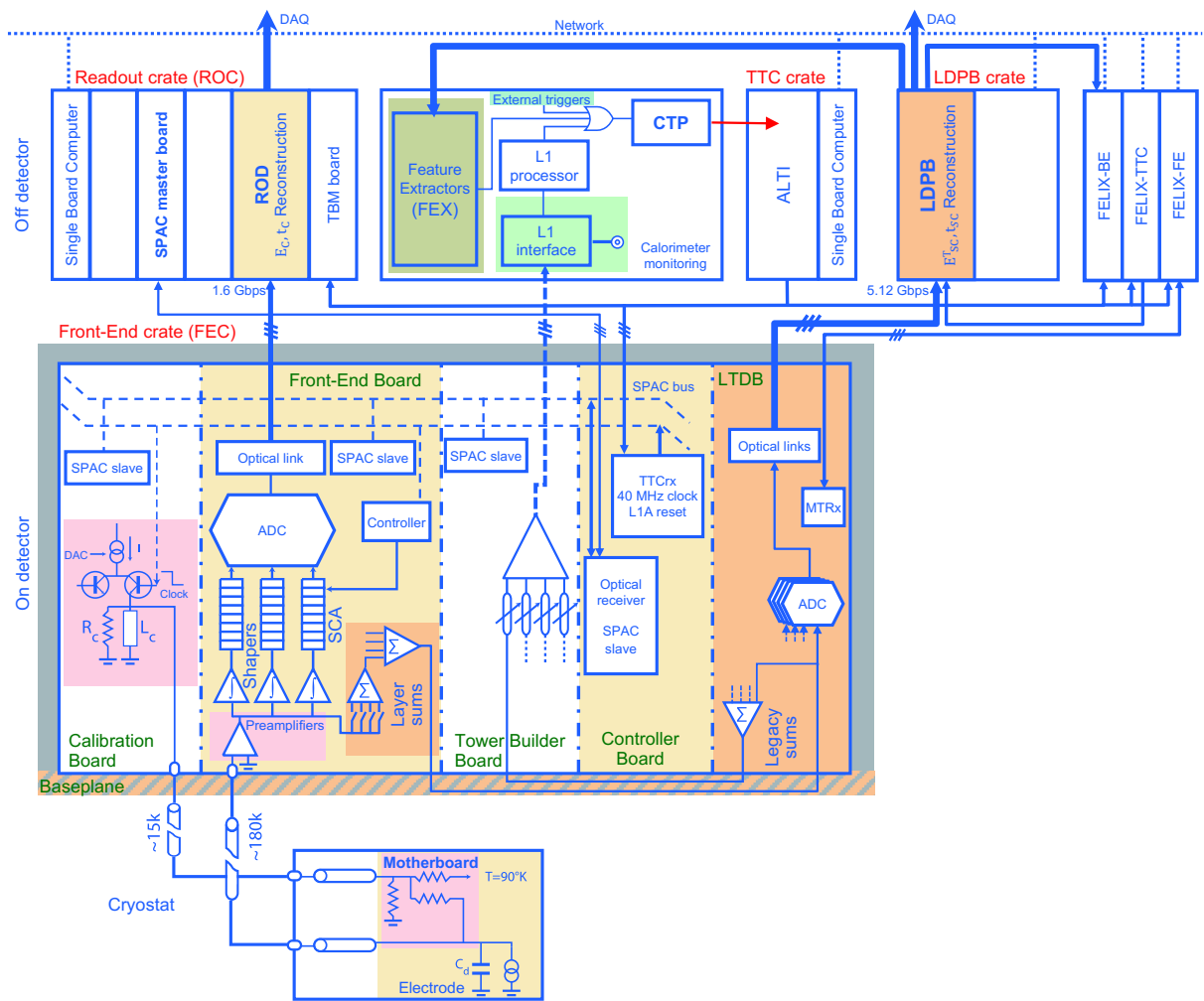


Figure 1: The ATLAS LAr calorimeter electronic architecture as of LHC Run 3. The new LAr boards are highlighted in orange. This diagram depicts the EM calorimeters; HEC and FCal electronics are slightly different.

part of the shaper chip located on the FEB motherboard, while the LSB is a plug-in card connected to the Linear Mixer.

Tower Builder Boards (TBBs): form the legacy Trigger Towers from the analog sums provided by the LSBs over the FEC baseplanes. The Trigger Tower analog signals are sent to the L1 trigger system via copper cables. In the HEC and FCal no further sums need to be produced after the LSB. Therefore, Tower Driver Boards (TDBs) are used in place of TBBs.

Calibration Boards: inject current calibration pulses whose shape is close to the pulse generated from the LAr ionization signal.

Controller Boards: receive the configuration and monitoring commands from the Serial Protocol for Atlas Calorimeter [8] (SPAC) masters installed in the Back-End Readout Crates. Controller boards receive also the Timing Trigger and Control [9] (TTC) signals coming from the Back-End TTC crates. They distribute the SPAC and TTC commands to the other legacy boards in the FEC.

Some FECs also host monitor boards transmitting the information from the sensors measuring possible mechanical stresses of the detector and the LAr temperature and purity. Another function of some of the monitor boards is to measure the status of the FECs' low-voltage power supplies. Each electronic board in a FEC is conductively cooled using two aluminium plates placed on each side of the board. These aluminium plates are part of a leak-less water cooling system.

On the Back-End side, two legacy systems are present:

Readout Crates (ROCs): Versa Module Eurocard (VME) crates hosting Readout Driver boards (RODs) that read the Analog-to-Digital Converter (ADC) data sent by the FEBs and compute energy (E_C) and time (t_C) for each cell signal at the L1 trigger rate. The ROCs also house the SPAC master boards and the Trigger Busy Modules (TBMs). The latter collect the busy signals from the RODs and distribute the TTC signals.

TTC crates: VME crates containing the modules that receive the TTC commands from the ATLAS Central Trigger Processor (CTP) system or generate locally these commands and transmit them to the other LAr boards.

The LAr electronics upgrade extends the legacy system with new Front-End components, sending the Super Cells' digital data to new Back-End components, which compute and transmit the Super Cells' E_T to the new trigger system. The architecture as of Run 3 is illustrated in Figure 1. This new LAr trigger readout system is composed of new Layer Sum Boards providing the analog sums for the higher trigger readout granularity; new baseplanes to route the increased number of analog signals and host the new LAr Trigger Digitizer Boards (LTDBs) that digitize the Super Cell analog signals at 40 MHz and provide the legacy sums for the TBBs; and new Back-End boards, the LAr Digital Processing Blades (LDPBs), that read the Super Cell ADC signals from the LTDBs, compute the Super Cells' E_T and send them to the new L1 trigger system. This new trigger system comprises a set of Feature EXtractors (FEX) with three subsystems targeting electromagnetic (eFEX), jet (jFEX) and global (gFEX) features [10]. The choice to convert the Super Cells' energy to E_T at the LDPB level was made to simplify the LTDB design. The LDPB is built in Advanced Telecommunications Computing Architecture (ATCA) format and comprises one ATCA carrier blade named LAr Carrier (LArC) and up to four Advanced Mezzanine Cards (AMCs) called LAr Trigger prOcessing MEzzanines (LATOMEs). The hardware control and monitoring of each blade proceeds via an Intelligent Platform Management Controller (IPMC) plugged into the LArC. In total, 124 LTDBs are installed on the 114 new baseplanes. Furthermore, 30 LDPBs corresponding to 30 LArCs and 116 LATOMEs, are installed in three ATCA shelves placed in one 19-inch rack. This new LAr system uses also three separate Front-End LInk eXchange (FELIX) [11] systems, comprising a total of 30 FELIX boards.

The new trigger readout path is illustrated in Figure 2 with solid red arrows. In order to ease the new system commissioning and have a fallback solution in case of unforeseen issues, the legacy trigger readout is kept functional since the LTDB sends the re-summed analog signals to the TBB, which will remain in operation during at least the initial phase of the LHC Run 3. The legacy trigger readout path is illustrated in Figure 2 with dashed red arrows.

Several other data paths are present in the system. A global monitoring path utilizes a Full Mode [11] data link between each LATOME and the FELIX system that connects to the ATLAS main data readout (path in orange arrows in Figure 2). Its purpose is to verify that the E_T sent to the trigger system is correct, by reading the Super Cell ADC data and the E_T values for all events selected by the first level trigger accept signal (L1A). Thus, this readout allows a recomputation of the calculation performed in the LATOME boards.

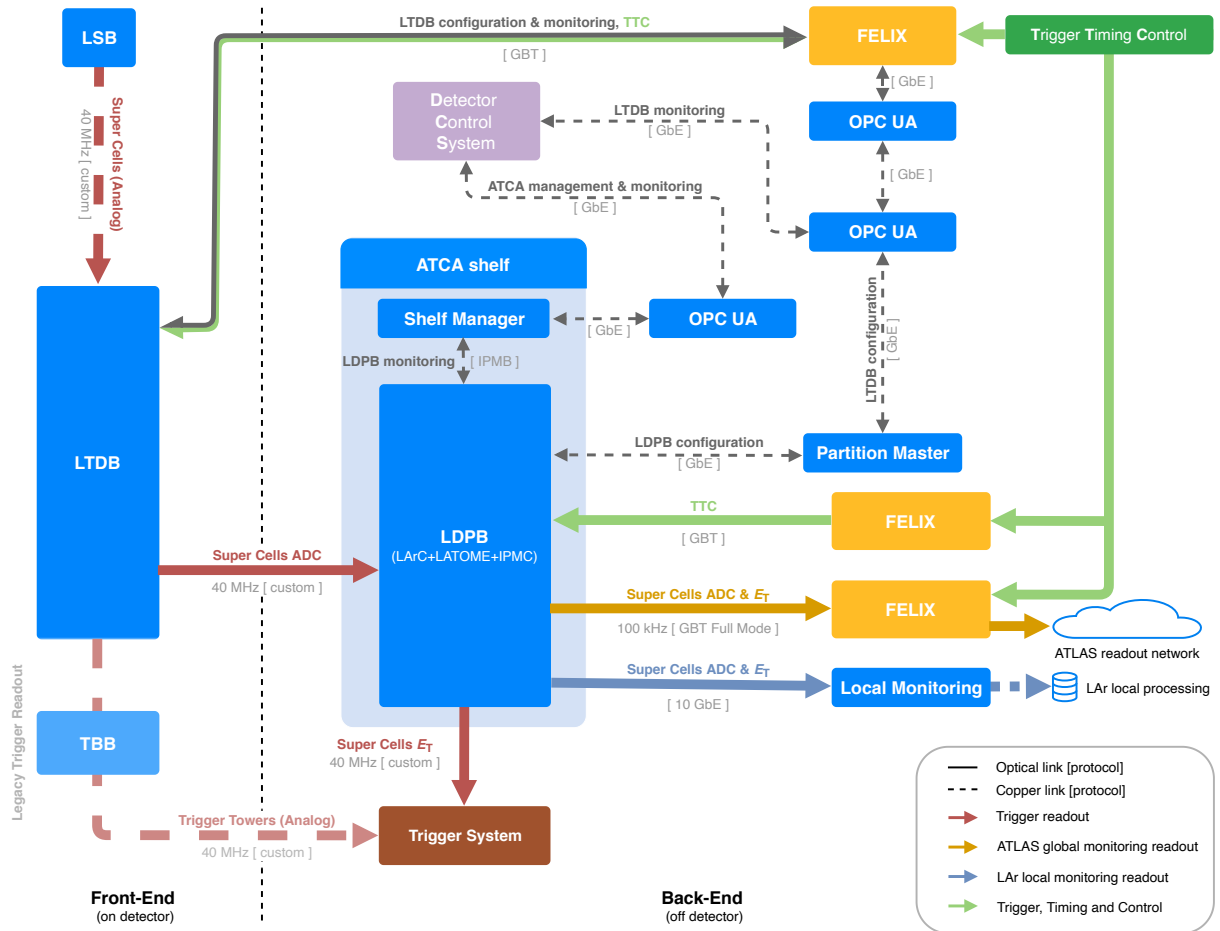


Figure 2: The ATLAS LAr calorimeter digital trigger readout system installed during the second LHC long shutdown.

A similar monitoring path utilizes the 10 Gigabit Ethernet (GbE) interface of the ATCA shelf that hosts the LDPBs (blue arrow in Figure 2). This readout is not connected to the ATLAS main readout but is used by a processing server specific to the LAr system. It enables a more flexible and localized monitoring to readout Super Cell ADC data and E_T at the L1A signal rate or optionally at any other rate, independently of the constraints present in the ATLAS main data readout in terms of bandwidth and event rate.

The whole system is synchronized with the TTC signals (green arrows in Figure 2). These signals provide the 40 MHz LHC reference clock, the L1A, the Bunch Counter Reset (BCR), the Event Counter Reset (ECR) and the Trigger Type commands. The BCR corresponds to the LHC orbit frequency and enables the determination of the collision time of an event via its Bunch Crossing Identifier (BCID). The ECR is used to compute an event identifier and the Trigger Type records which subsystem issued the L1A. The TTC signals are transmitted to LTDB and LDPB through FELIX systems with Gigabit Transceiver (GBT) [12, 13] links.

The configuration of the LTDB and LDPB hardware proceeds via a "Partition Master" PC. This computer is connected to LTDBs in three stages: two Open Platform Communications Unified Architecture (OPC UA) servers and a FELIX system, connected to LTDBs via GBT links. The first OPC UA server takes care of the LTDB configuration command generation, according to the run control commands received from the

Partition Master. The second OPC UA server packs these specific commands to follow the GBT protocol. The Partition Master connection to the LDPB is made directly via a 1 GbE interface.

A Detector Control System [14] (DCS) handles the hardware monitoring: it ensures that the hardware is operated under safe conditions and provides basic safety mechanisms in case of failure. The connection to the LTDB is made with a part of the same OPC UA and FELIX chain used for the configuration. The LDPB is connected to the DCS via an OPC UA server and the ATCA shelf manager, interfaced to the IPMC on the LDPB via an Intelligent Platform Management Bus (IPMB).

Some differences exist in the signal processing between the main and trigger readout systems: the analog signal processing in the main readout comprises pre-amplification followed by shaping performed in three different gain scales, such that three overlapping gains are obtained with a ratio of about 10. The bipolar shape is created with a time constant of 13 ns. The samples stored by the Switched Capacitor Array (SCA) analog pipeline chip are digitized by a 12-bit ADC and sent to the Back-End system via a 1.6 Gigabit per second (Gbps) optical link. In the trigger readout, the analog processing has a similar shaping with only one gain scale, but with a special conditioning described in Section 3.3.3. The Super Cells' digital samples generated in the LTDBs are sent to the Back-End system with a 5.12 Gbps optical link. While in the main readout the RODs compute the cell energies and signal times at the L1A rate (up to 100 kHz), the LDPBs of the trigger readout compute the Super Cell transverse energies (E_{SC}^T) and signal times (t_{SC}) at the LHC collision rate (40 MHz).

The new trigger readout aims to have an Integral Non-Linearity (INL) for each Super Cell channel below 1% with a Super Cell energy computation precision below 250 MeV. Even under high pile-up data taking conditions, this computation must remain unbiased.

In the following, the new hardware, as well as the procedures carried out to validate its functionalities, are described in detail.

3 New Front-End electronics

3.1 Baseplanes

At each end of the barrel cryostat 32 calorimeter signal feedthroughs [15] are installed, distributed around the cylindrical periphery at nearly uniform angles. Each of the two end-cap cryostats has 25 signal feedthroughs distributed around the far end (from the collision point) of its periphery. Each feedthrough with cold and warm flanges connected via vacuum cables is made up of four pin carriers. Each pin carrier has either seven or eight connectors and each connector has 64 signal pins. A pedestal spans two adjacent feedthroughs and a FEC is mounted on each pedestal. Each FEC is divided into two halves with a baseplane installed in each half for almost all of the crates, see Figure 3. For each connector in a pin carrier a flex ribbon cable carries 64 signals from the feedthrough to a connector on the back side of the baseplane. The pins in this connector extend through to the front side of the baseplane. A FEB has two 64-pin signal connectors and this board, mounted in a FEC, plugs into the baseplane. Between the two signal connectors on each FEB is a third 64-pin connector, which returns analog trigger signals to the baseplane where they are routed to trigger-handling boards, also plugged into the baseplane.

For the Phase-I upgrade, new baseplanes are required (1) to accommodate the finer trigger segmentation, (2) to make room for the LTDBs (Section 3.3), and (3) to maintain the legacy Level-1 trigger system. The new mezzanine LSBs (Section 3.2), mounted on the existing FEBs, provide more analog signals than

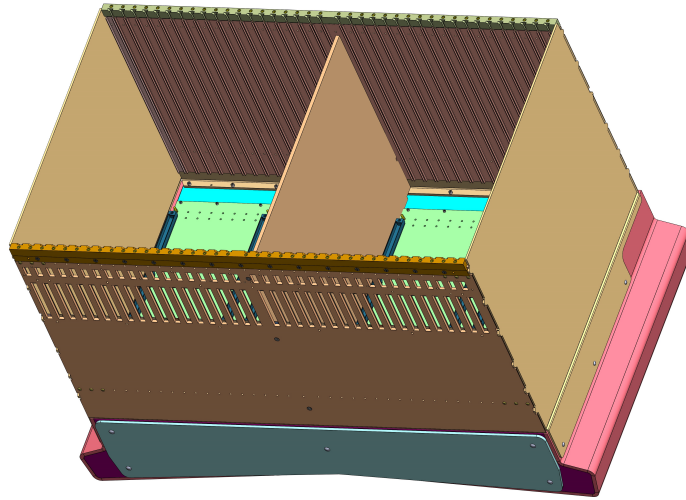


Figure 3: Perspective drawing of a FEC mounted on its pedestal. Simplified sketches of the two baseplanes can be seen mounted on the pedestal inside the crate.

before onto the baseplanes, which are now routed to both the LTDBs and to the existing TBBs or TDBs requiring additional signal layers on the baseplane Printed Circuit Boards (PCBs). Because the LTDB baseplane connectors are wider than those for the other boards plugged into the baseplane, there is no space next to an LTDB for the Radio Frequency (RF) shields which protect the small-signal inputs to the FEBs from extraneous noise. This requires, in some cases, additional slots and/or significant re-arrangement of the baseplane slot assignments, as well as thicker baseplane PCBs, whose thickness is highly constrained by the existing size of the FEC and FEBs. Table 1 gives an overview of the physical dimensions of the various baseplane types.

The new EMB baseplane has the same number of slots (19) as the original baseplane. Space for the single new LTDB comes from a previously unallocated slot at one end of the FEC. Some FEBs have been shifted by one slot to allow the LTDB to sit in the middle slot of the baseplane next to the TBB (see Figure 4). The flex ribbon cable connections underneath the baseplane are then also shifted by the same amount.

The EMEC crates house two different types of baseplanes. The EMEC standard crate has baseplanes similar to the EMB but with one fewer FEB, leaving a slot for an additional monitor board. The EMEC

Table 1: Overview of the number of PCB layers, physical dimensions and numbers installed on the detector for the various baseplane types. Side A and side C are oriented along the positive and negative z -axis of the experiment.

	EMB	EMEC Standard	EMEC Special	HEC	FCAL side A	FCAL side C
PCB layers	12	12	14	12	16	16
Length [mm]	388.00	388.00	522.73	260.00	450.60	490.00
Width [mm]	415.00	415.00	415.04	415.00	406.40	406.40
Thickness [mm]	2.40	2.40	2.36	2.36	2.36	2.36
# on detector	64	32	8	8	1	1

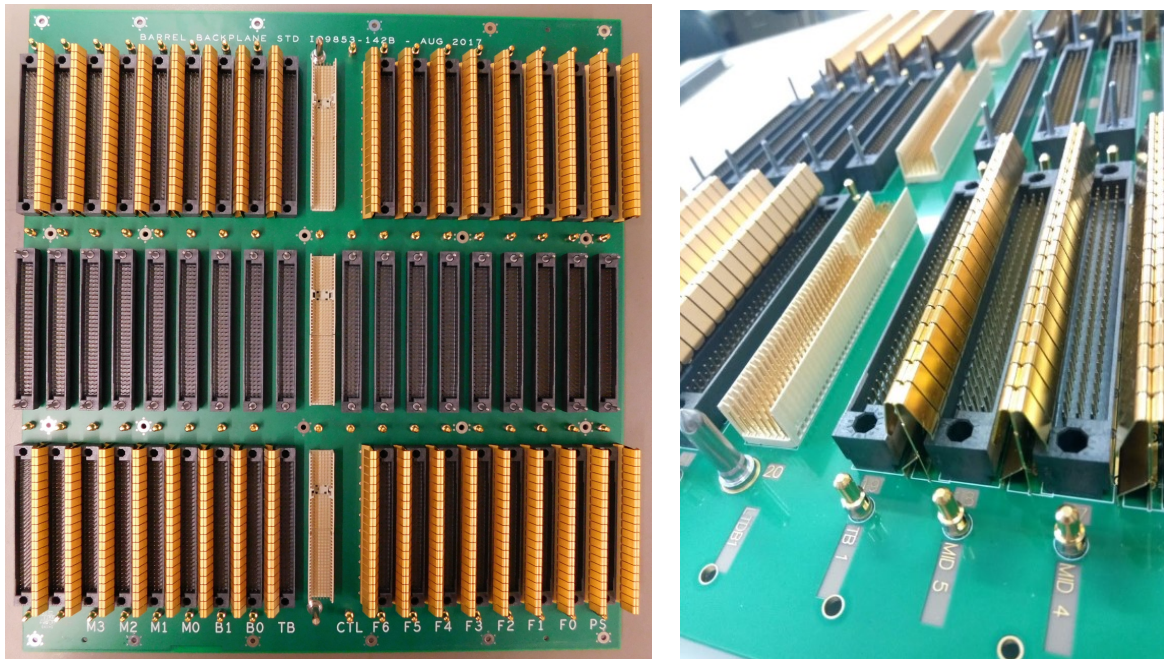


Figure 4: Left: Photograph of an EMB Baseplane. The slot with three wider baseplane connectors is for the LTDB. Just to the left of the LTDB is the slot for the TBB and to the right is the Controller board slot. The calibration board slot is on the far left and next to it is the monitor board slot. The gold-colored RF shields surrounding connectors in the top and bottom rows identify the FEB slots. Right: Close-up of an EMEC special baseplane showing the RF shields and the wider LTDB connectors.

special crate has one baseplane for the EMEC and another for the HEC. The EMEC special baseplane has two LTDBs and it extends well beyond the center of the crate. The HEC baseplane in the other side of the crate consequently has room for only 13 slots rather than the normal 19 slots of the EMB baseplanes and the EMEC standard baseplanes. An overview of the different boards which plug into the various baseplane types can be found in Table 2.

The original FCal baseplanes had 19 slots, each fitting within one-half of a FEC. The other half was used for devices which monitor the status of the cryostats. The new FCal baseplanes each have two LTDBs and the baseplanes extend two (three) slots into the now unused other half crate for the A-end (C-end). Integrated into each new FCal baseplane are traces carrying pulses from the calibration board through attenuating injection resistors (surface mounted on the backside of the baseplane) to those pins on the baseplane connectors which carry FEB signals.

Prototype and production baseplanes were subjected to a series of tests. For those connector pins which are specified to be grounded, the impedance to ground was confirmed to be consistent with zero. Likewise, connector pins which are not specified to be grounded were also checked. The impedance of traces on the baseplanes was measured with a time-domain reflectometer. Continuity between trace ends was compared with the net lists. These mapping tests were then compared with independent LTDB mapping requirements. Signal integrity on the traces and cross-talk between near-by traces were measured with a pulser and oscilloscope to verify that they met specifications. In the case of the FCal baseplanes, the calibration injection resistors were all measured for correct values. All baseplanes were shown to meet the specifications.

Table 2: Overview of the different board types which plug into each of the baseplane types.

	EMB	EMEC Standard	EMEC Special	HEC	FCAL
FEBs	14	13	17	6	14
LTDBs	1	1	2	1	2
TBBs	1	1	3	0	0
TDBs	0	0	0	2	2
Calibration	1	1	2	1	1
Controller	1	1	1	1	1
Monitor	1	2	0	0	1
Low Voltage Power	0	0	0	2	0
Total	19	19	25	13	21

3.2 Layer Sum Boards

In the LAr trigger readout, the first level of summing is provided by the Linear Mixer, which sums over four channels in azimuth with different gains in different regions of η . The upgrade to the trigger branch begins with the output of this signal. The LSB is a plug-in card for the FEB that performs a second level of summing of the analog signals [16]. There are two LSBs mounted on each FEB. For the Phase-I upgrade, the new LSB output provides signals for the finer granularity Super Cells in the front and middle layers, while retaining the signals needed for the legacy trigger path elsewhere. Six main types of new LSBs have been produced:

S2x8 The basic circuit on the board performs an analog sum of two input channels from the Linear Mixer. There are eight copies of this circuit on each LSB. There are 896 boards of this type required for the EMB and 192 for the EMEC, with 288 reused from the original construction.

S2x8D S2x8 LSBs were already used in the back layer of the EM calorimeters. For Phase-I, this output signal must be sent to both the new LTDB and the legacy TBB. A simple splitter is added to the S2x8 in order to produce this dual output. There are 128 boards of this type required for the EMB and 160 for the EMEC.

S1x16LN This LSB has no summing function and only serves as a line driver for the Linear Mixer signal. There are sixteen copies of this circuit on each LSB. There are 448 boards of this type required for the EMB and 544 for the EMEC.

S1x12+S6x2 For the front section of the EMEC in the range $1.8 < |\eta| < 2.0$, the output from the shapers covers the area $\Delta\eta \times \Delta\phi = 0.0167 \times 0.1$. These are sent individually to the LTDB, while sums of six inputs are sent to the TBB. There are 128 boards of this type required for the EMEC.

S2x6D+S1x4 At the end of the EM Barrel ($|\eta| > 1.4$), each LSB must handle four signals originating from the middle layer and 12 signals from the back layer. The signals from the back layer are summed and handled with the same circuitry as the S2x8D and sent to the LTDB and TBB, while the four signals from the middle are just passed directly to the LTDB as in the S1x16LN circuit. There are 128 boards of this type required for the EMB.

FCal All the LSBs above form an unweighted sum of cells in a narrow region of η , while in the FCal, one must perform a sum over a relatively wide range in pseudorapidity, over which the conversion factor from energy to transverse energy varies significantly. For this reason, the inputs to be summed on the FCal LSBs are weighted to perform the conversion to transverse energy before summing. This leads to a large variety of LSBs, which, within a given FCal module, differ only by the weighting resistor values. All 56 FCal LSBs were replaced by the new design.

The technical specifications for all the boards are that the gain should not vary by more than 2% from nominal, the summing amplifier INL should be $< 1\%$, and the Direct Current (DC) offset should be $< 2\%$ of the maximum output voltage. All boards were tested before and after a week-long burn-in. About 99% passed the specification and were delivered to CERN. As the replacement of the baseplanes required that all electronics in the FECs be disconnected and removed, all FEBs were brought to a surface laboratory. Here, the FEBs were “opened” (i.e. the cooling plates dismantled) and the LSBs replaced by the new boards. Figure 5 shows a photo of an example LSB.

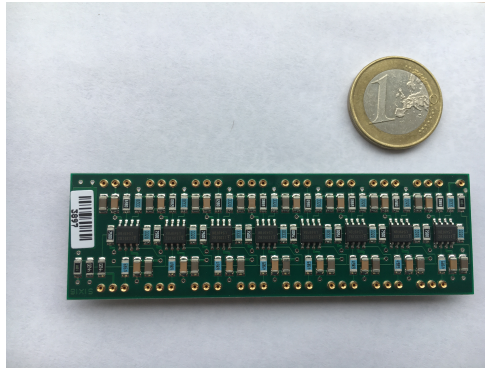


Figure 5: Photo of an S1x16LN LSB. Only one side is shown. Half of the components are on the other side. A one-euro coin is shown for scale.

3.3 LAr Trigger Digitizer Boards

An LTDB processes and digitizes up to 320 Super Cell signals (“channels”) and transmits them via optical links to the Back-End, while also providing summed analog legacy signals for the TBB via the new baseplanes. The following sections describe the key ASICs for digitization and optical transmission, the motherboard that houses them, the mezzanine card providing the power, quality assurance and control for the assembled system as well as considerations on compatibility with the Phase-II upgrade.

3.3.1 Analog-to-Digital Converter

A custom, quad-channel, pipeline ADC was designed to process the shaped analog signals from the LAr calorimeter Super Cells. These signals are continuously sampled and digitized at 40 Megasamples per second. To digitize the energy of the trigger signals, the ADC has a dynamic range of approximately 12 bits (after calibration) with a required precision of at least 10 bits [1]. Each ADC consumes 45 mW per channel and has a latency of less than 125 ns, meeting the power and latency budgets at the system level of less than 145 mW per channel and 200 ns, respectively.

Radiation tolerance is a key requirement for the ADC, as it is for all devices located on-detector and within the substantial radiation field. The device must operate reliably through the remaining LHC run, as well as the High Luminosity LHC (HL-LHC) runs, with a total expected integrated luminosity of 3000 fb^{-1} , possibly up to 4000 fb^{-1} . This places strict requirements on the ADC, particularly for the tolerance to total ionizing dose (TID) and single-event effects (SEE), which depend on the expected level of radiation at the readout electronics location [17]. The LAr on-detector ASICs are required to be radiation tolerant up to a total ionizing dose of 180 kRad, non-ionising energy loss doses of up to $4.9 \times 10^{12} \text{ n eq/cm}^2$, and be relatively unsusceptible to (recoverable) SEEs for a total fluence of up to $7.7 \times 10^{12} \text{ hadrons/cm}^2$ [18].

The ADC chip consists of four identical ADC channels and is implemented in CMOS 8RF 130 nm technology. Each channel consists of a multiplying digital-to-analog converter (MDAC) pipeline followed by a successive approximation (SAR) ADC, as shown in Figure 6. The MDAC pipeline contains four 1.5-bit stages, each with a nominal gain of two. The additional half-bit overlap allows for a digital on-chip calibration to correct capacitor mismatch. These stages resolve the four most significant bits [19]. The remaining eight least significant bits are resolved by the SAR stage. An internal Phase Lock Loop (PLL) generates a 640 MHz clock from a 40 MHz input clock (provided by the LTDB), of which both edges are used for the SAR operation. The MDAC stages operate with a supply voltage of 2.5 V and a common-mode voltage of 1.25 V, while for the SAR a supply voltage of 1.2 V with a common-mode of 0.6 V is used [20]. A digital data processing unit (DDPU) applies the calibration, forming the digital output, and the data are serialized and sent off the chip over a Scalable Low-Voltage Signaling (SLVS) driver at 320 MHz. An Inter-Integrated Circuit (I^2C) interface is used for chip control. An image of the chip layout is shown in Figure 7.

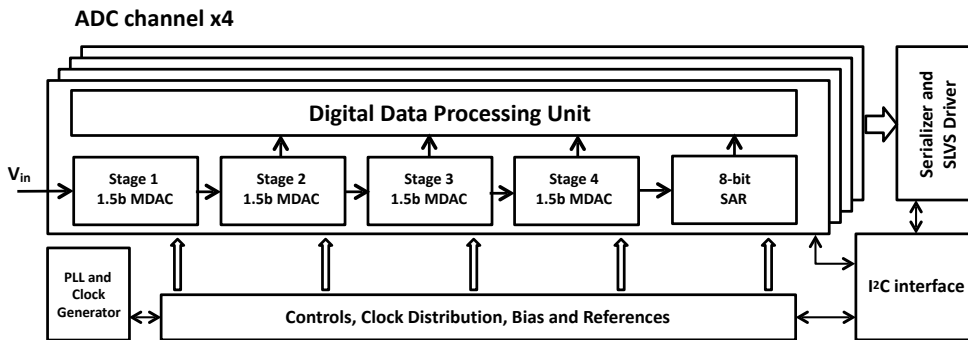


Figure 6: ADC block diagram.

The 130 nm CMOS 8RF technology does not have sufficient fabrication accuracy to meet the 10 bit precision specification. Therefore, a digital calibration is performed to correct for capacitor mismatch in the MDAC stages. The algorithm measures the actual gain and compares it to the ideal MDAC gain of exactly two. The difference is then taken as a correction and applied to the digital output in the DDPU. By design, the gains are lower than two to avoid over-ranging the input to the following stage, which would lead to missing codes. This results in a reduction of up to 10% of the dynamic range of the chip with respect to the nominal 12 bits (or 4096 counts), within the margin of acceptable performance. The calibration constants are calculated off-line but stored on-chip and must be reloaded to the chip after power cycling.

The radiation tolerance of the ADC chip has been studied in its different prototyping stages. The TID and SEE tests performed with a proton beam at the Francis H. Burr Proton Therapy Center at Massachusetts General Hospital with prototypes are described in references [19] and [21]. Radiation tolerance was

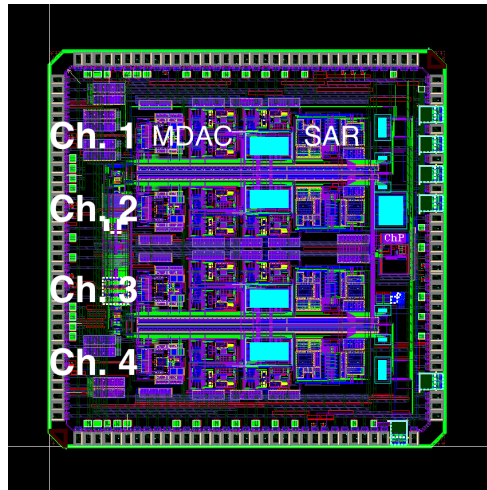


Figure 7: Image of ADC layout (3.6 × 3.6 mm).

established for a TID of up to 10 MRad and for non-ionising energy loss up to a fluence of the order of 10^{14} n eq/cm². Proton SEE cross-sections were measured to be of the order of 10^{-12} cm² per ADC channel. In addition to the proton radiation tests, SEE cross-sections were measured using four different species of heavy ions at the Cyclotron Resource Centre at Louvain-la-Neuve, Belgium, targeting a larger range of deposited energies and complementing the existing studies with protons [20].

To equip the 124 LTDBs approximately 12000 fully functional ADC chips were required (80 chips per LTDB, plus spares). Allowing for yield factors 17200 chips were produced and packaged in molded QFN-72 packages. The individual ADCs were tested using a socketed test board which allowed for a sine wave input, low-jitter clock, power and readout via a Field Programmable Gate Array (FPGA). The functionality, dynamic range and precision, evaluated by the effective number of bits (ENOB), were measured. A total of 12838 chips were identified as having four channels with a dynamic range greater than 3600 counts and an ENOB larger than 9.9 bits (using the limited-precision socketed board) [20], and thus were qualified to be used for LTDB production.

3.3.2 Serializer and optical transmitter

The digitized signals from up to 320 ADC channels per LTDB in the format of serial bit streams at 640 Mbps are prepared for uni-directional, high-speed serial-data transmission over fiber optics using the link-on-chip (LOC) serializer ASIC named LOCx2 [22]. Each LOCx2 can process the data from four ADC chips (a total of 16 ADC serial output channels) for transmission of the data via two 5.12 Gbps optical links to the Back-End. Five bi-directional 4.8 Gbps control links provide configuration, control and monitoring based on the GBT serializer-deserializer ASIC GBTx [23]. Consequently, each LTDB has up to 40 fibers for the data links and ten fibers for the control links, with all 124 LTDBs installed in ATLAS comprising a total of 5848 fibers and a throughput of more than 29 Tbps for the whole optical link system. The Miniature Transmitter (MTx) and Miniature Transceiver (MTRx) [24] are the optical transmitter and transceiver developed to fit between the LTDB PCB and the cooling plate with a clearance in thickness of six millimeters. The MTx is based on the LOCld [25] laser driver ASIC and an 850 nm Vertical Cavity Surface Emitting Laser (VCSEL). The MTRx uses the GBTIA [26] ASIC-loaded Receiver Optical Sub Assembly (ROSA) from CERN for the receiving channel. All ASICs and the optical components are tested

to be radiation tolerant for applications in the LAr FECs [1, 17, 27]. The design of the two links, including the choice of the fiber, follows the guidelines of the Versatile Link collaboration [28]. Figure 8 shows a block diagram of the data and control links.

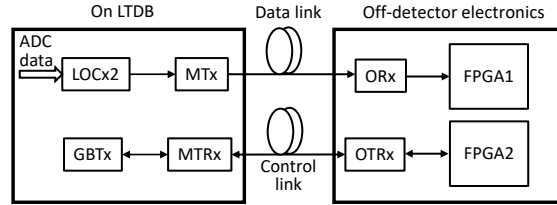


Figure 8: Block diagram of the LTDB optical links.

As the data link transmits information for the ATLAS Level-1 trigger, it is crucial that the transmission latency is fixed and is within the time budget of the ATLAS trigger system. This requirement, after subtracting the signal propagation in the optical fiber, translates to a maximum latency of 75 ns for LOCx2 [1].

The LOCx2 and LOClD ASICs are specifically designed for the LTDB and are based on commercial silicon-on-sapphire 250 nm CMOS technology. The two LOCx2 5.12 Gbps serializer channels share one high-speed clock system based on an inductor-capacitor (LC) oscillator PLL. They use a low-overhead custom encoding and framing transmission protocol (LOCic [29]) developed to meet the requirement of transmission latency, and to achieve automatic link re-synchronization should the receiving end of the link fail to recognize the transmission frame due to single event upset (SEU) in the link Front-End. The encoding protocol can detect up to three consecutive SEU errors, enabling the link Back-End to discard data containing SEU errors. The LHC bunch-crossing ID is embedded in the protocol to save transmission bandwidth. The LOCic also scrambles the data to achieve DC balance in data transmission through fibers. The LOClD is the matching dual-channel VCSEL driver for the LOCx2. Figure 9 shows the block diagram of the LOCx2.

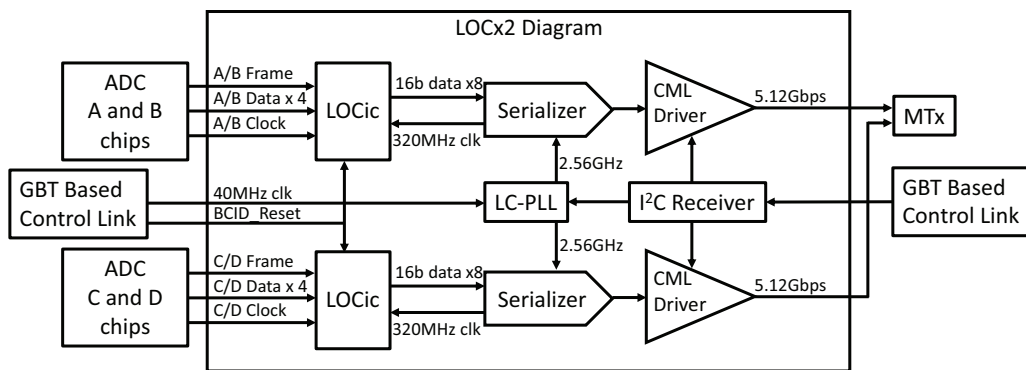


Figure 9: LOCx2 block diagram with connections to four ADCs (A,B,C and D), Control Link and MTx.

MTx and MTRx share the same mechanical design and electrical connector. A custom mechanical coupler (the “Latch”) holds the fiber and the Transmitter Optical Subassembly (TOSA) or ROSA together. The

fiber couples with the TOSA or ROSA through an industry standard ferrule. Figure 10 shows a photo of an MTx with the custom Latch to achieve the overall module height of 6 millimeters.

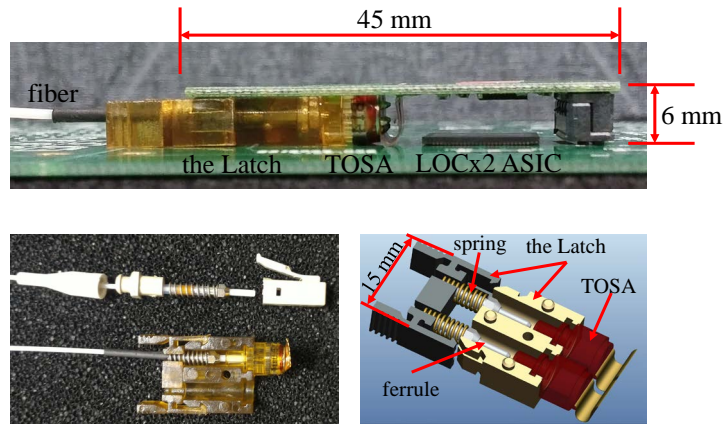


Figure 10: MTx and the Latch that couples the fiber with the TOSA or ROSA. Top: MTx on the LTDB with the LOCx2 under the module to save PCB space on the LTDB. Lower left: the LC ferrule taken from the industry standard LC fiber connector and the injection molded Latch. Lower right: a computer-aided design diagram of the Latch with the spring and ferrule to couple with the TOSA.

3.3.3 Motherboard

The LTDB motherboard digitizes the Super Cell signals from the FEBs, and sends the data to the Back-End electronics for trigger processing. Each LTDB is powered by a plug-in Power Distribution Board (PDB, see Section 3.3.4) and can receive up to 320 Super Cell signals which are amplified by commercial amplifier chips and digitized by the custom ADCs. The digitized data are then packaged and serialized in the LOCx2, and sent out through 40 optical fibers, where each fiber transmits the data at 5.12 Gbps. For Super Cell signals from the front and the middle layers, four neighboring signals are summed up, and the resulting 64 summed signals on the LTDB are sent to the legacy TBB through the new baseplane. Each LTDB comprises five independent identical logical groups, every one capable of processing up to 64 Super Cell signals with 16 ADCs, four LOCx2 and four MTx. One GBTx set per group implements timing, control and monitoring. A block diagram of the LTDB is shown in Figure 11, and the data flow and control links are shown in Figure 12. While many elements of the LTDBs (such as powering) are common to all channels and consequently represent single points of failure for all channels, the independent logical groups enable normal operation of the other sections in case of a component failure in one section.

Timing, control, and monitoring are implemented through five GBTx links which operate at 4.8 Gbps in both directions to communicate with the FELIX system. The GBTx chips receive timing and control information through the down-link from the FELIX, then fan-out the clock signals to each ADC, and distribute the clock and BCR signals to each LOCx2 as illustrated in Figure 13. The control commands are transferred to GBT-SCA (Slow Control Adapter) [30] chips, then to be used to configure the MTRx, MTx, ADC and LOCx2 ASICs through the I²C bus, and reset the ASICs through the General-Purpose Input/Output (GPIO) ports.

The monitoring information, including voltages, currents, temperatures and power module status are transferred to the FELIX through the LTDB up-link. There are four input power rails drawn from the

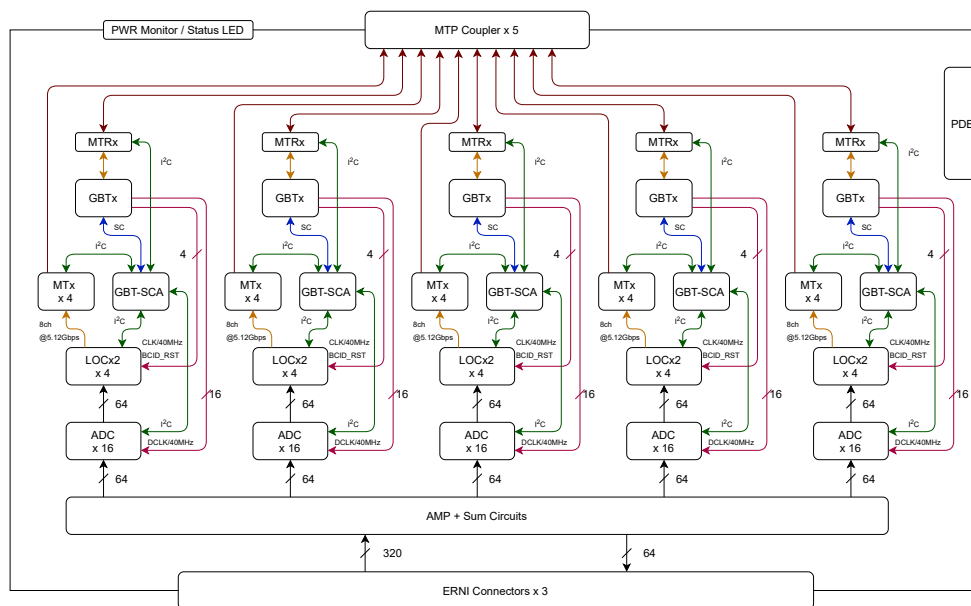


Figure 11: Block diagram of the LTDB: the board can be divided into five groups. Each group processes up to 64 Super Cell signals with 16 ADCs, four LOCx2 and four MTx. There is one GBTx set to implement timing, control and monitoring per group.

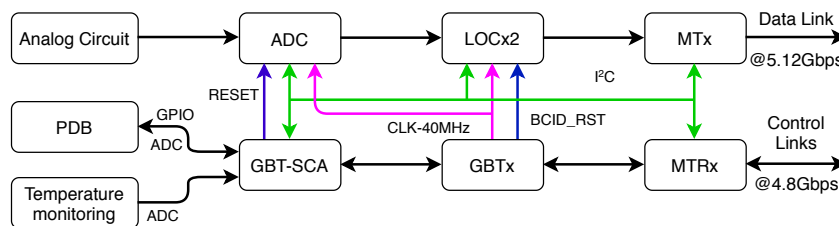


Figure 12: Block diagram of the LTDB data flow, showing the data link and the control link. The data link proceeds from the Super Cell signals injected into analog circuitry to ADC, LOCx2, and transmission through MTx. The control links send the clock and commands to GBTx, and collect monitoring information through MTRx.

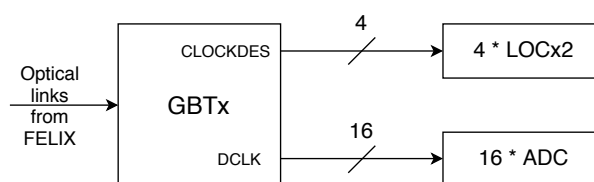


Figure 13: Block diagram of clock distribution on the LTDB. The DCLKs of the GBTx are used for the ADCs, and the CLOCKDES clocks of the GBTx are used for the LOCx2 chips.

power bus of the FEC that are used to provide power to the LTDB. A shunt resistor installed in each power rail allows the monitoring of both current and voltage. There are also ten thermistors to measure the board temperature in different positions on the LTDB. All this monitoring information is collected through the ADC of the GBT-SCA. The power modules on the PDB have “Power-Good” signals that are used to indicate their operational status. These Power-Good signals are collected through the GPIO or the ADC of the GBT-SCA.

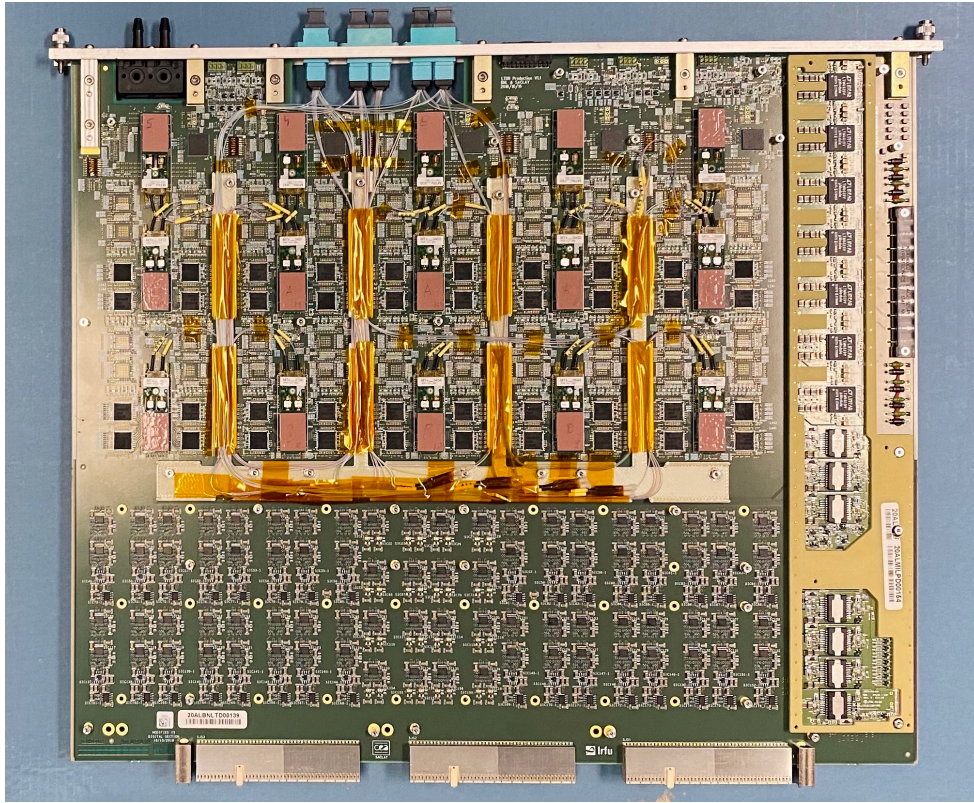


Figure 15: Photograph of an assembled LTDB with PDB installed.

This conversion and the dynamic range matching are done by a very low-power (1.14 mA/channel) fully-differential amplifier (THS4522), equipped with an appropriate passive network to set the gain and the pedestal at the ADC input.

In the case of the main readout, the current pulse coming from the cells is shaped by a CR-RC² filter. This filter is optimal in terms of signal over noise optimization. In the case of the trigger path, the cell signals are first summed in groups of up to four cells by the Linear Mixer, and shaped by a CR-RC active filter. A CR-RC filtering has been chosen to minimize the attenuation over the trigger path, and a passive RC stage with a time constant of 15 ns is implemented on the LTDB to get the same optimal CR-RC² as for the main readout. This passive RC stage also acts as an anti-aliasing low-pass filter in front of the LTDB ADC. Super Cell signals corresponding exactly to legacy analog trigger signals are configured as a high impedance pick up on the LTDB, since they are directly sent via the backplane to the legacy analog trigger boards (TBB and TDB), whose inputs are 50 Ω adapted. Super Cell signals that need further summing on the LTDB before being sent back to the backplane for the legacy analog trigger, are 50 Ω adapted on the LTDB.

The Linear Mixer is no longer in its linear dynamic range if its output amplitude goes above 3.3 V. This voltage threshold has to match the 2.4 V saturation voltage of the ADC differential input. Since each ADC has 3600 to 3800 available digital codes, the least significant bit of the LTDB ADC corresponds approximately to 1 mV at the Linear Mixer output everywhere on the detector.

In addition, the pulses from the Super Cells do not all have the same shape, since the drift time of the charges produced by ionization of the Liquid Argon by the shower particles changes as a function of η . Because a bipolar shaping circuit is used, this translates into a change of the amplitude of the undershoot

of the pulse. Since the undershoot has to be digitized and should not saturate the ADC, the gain and pedestal of each channel have been adjusted so that signals close to the Linear Mixer saturation amplitude use the full dynamics of the ADC input. Over the whole acceptance of the calorimeter, this leads to gain differences up to 30%.

3.3.4 Power distribution board

Power distribution on the LTDB is provided by the PDB mezzanine card. The choice of developing a separate board for the generation of the supply voltages for the LTDB ensures forward compatibility in the future Phase-II upgrade, for which a different power distribution scheme for the Front-End electronics is planned. The use of a mezzanine board allows the re-design and replacement of only the PDB, without modifying the LTDB itself (as explained in Section 3.3.6).

The PDB consists of digital and analog sections to power the corresponding sections of the LTDB. The block diagram of the power scheme is shown in Figure 16. From the +6 V line taken from the FEC power bus, the following voltages are created for the digital part of the LTDB: +1.2 V, +1.5 V, +2.5 V and +3.3 V. This is achieved using LTM4619 DC-DC converters from Linear Technology Corporation (now Analog Devices, Inc.).

The analog voltages are generated as follows. From the +7 V (-7 V) of the FEC power bus, the +5 V (-5 V) is generated using the LHC4913 (LHC7913) Low-DropOut (LDO) linear voltage regulators from STMicroelectronics. The LHC4913 is also used to generate the analog +2.5 V, starting from the +6 V of the power bus (with an intermediate step down at +4 V, using an LTM4619, to avoid a large voltage drop in the LDO).

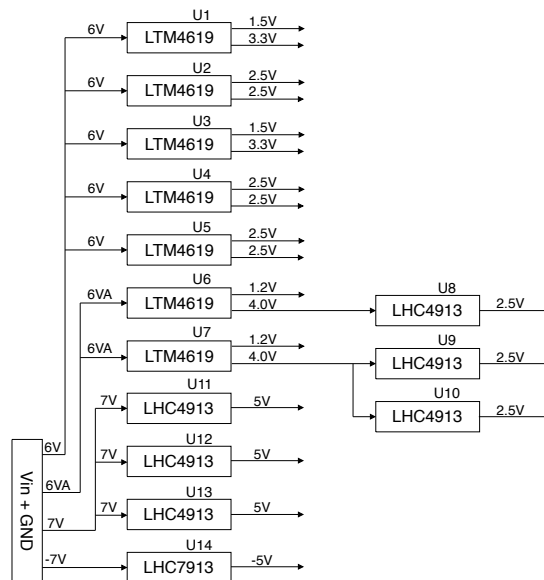


Figure 16: Power scheme of the PDB. The board integrates LTM4619 DC/DC converters (U1-U7) and LHCx913 linear voltage regulators (U8-U14) to produce the voltages needed by the LTDB (the number of devices has been established based on the budget of the output currents). From the two +6 V lines available on the input power bus, one (labelled "6V") is used to generate the digital voltages and the other one ("6VA") is used to generate the analog voltages (see text).

The PDB is radiation tolerant [32–34] and able to operate in presence of the maximum magnetic field expected in the LTDB positions (lower than 0.1 T) [35]. The radiation tolerance requirements for the PDB are less stringent than for the rest of the LTDB components (see Section 3.3.1) since the board will have to operate only for the LHC Run 3 and will be replaced before the start of the HL-LHC.

The board is manufactured as a ten-layer PCB of 1.6 mm thickness², reinforced with a fiberglass (G10) frame glued on the top side. When mounted on the LTDB motherboard, the total maximum vertical height is about 5.4 mm, which fits just below the LTDB cooling plate, mounted at 6 mm from the motherboard surface. A picture of one production PDB is shown in Figure 17. An automated set-up has been developed to test the correctness of all output voltages of the PDBs at full load before they were shipped to the LTDB assembly sites.

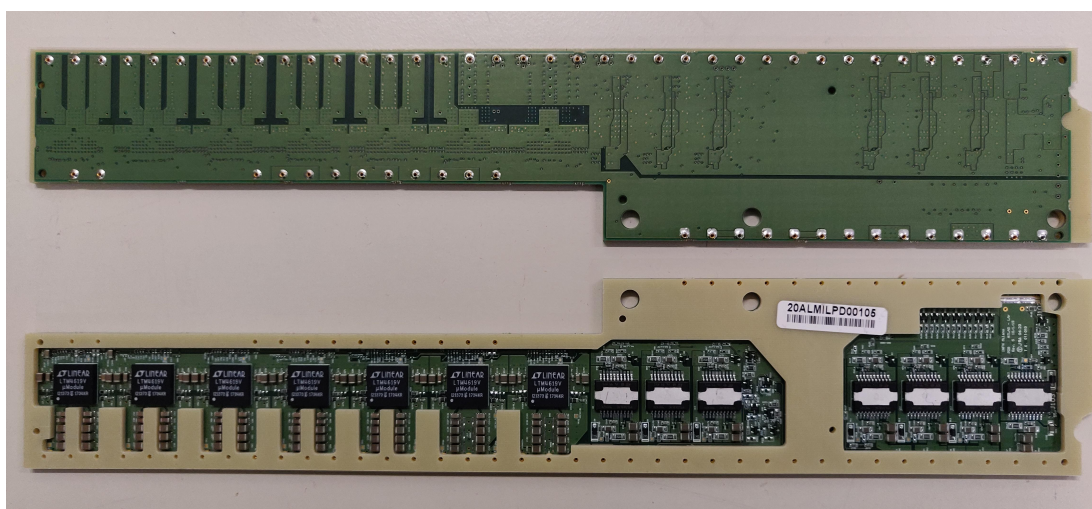


Figure 17: Picture of a PDB as seen from the bottom and top. All components are mounted on the top side. On the same side, the G10 reinforcement frame is also visible.

3.3.5 Quality assurance and control

The LTDB quality assurance and control (QA/QC) involves the testing of three main components: the cooling interface is tested for leaks, the PDBs are tested to meet the requirements on voltage and current of the outputs, and each LTDB with a qualified PDB installed is subjected to functionality testing and – integrated with the test stand – to performance testing as detailed below.

Each PDB module is tested with a standalone test stand to verify basic functionality before it is cleared to be installed on an LTDB motherboard. The input and output voltages and current are measured to obtain efficiency information. All test data and analysis results are examined and logged into a database. A PDB module is accepted if it passes the following requirements: the output voltage is within $\pm 2.5\%$ of the nominal value; the output voltage ripple is within 10 mV peak-to-peak; and the efficiency is better than 70% at nominal load.

The PDBs passing the tests above are then subjected to a Highly Accelerated Stress Screening (HASS) test, where the PDBs are placed in a chamber and undergo ten thermal cycles between 0 °C and 60 °C for about

² The PDBs have been produced by ARTEL S.r.l. - 52041 Pieve Al Toppo (AR) - Italy

12 hours. The goal of the HASS test is to find any failures due to component infant mortality, cold solder joints, etc. After HASS testing, each PDB is installed on an LTDB for re-testing, where the voltage of all outputs is measured, control and monitoring signals are tested, and the power rail ramp-up time (from 10% to 90% of the rising edge) for the GBTx is measured as well. If the PDB passes this re-testing, it can be used on the LTDB for integration testing.

Each LTDB motherboard is initially tested with a standalone test stand to verify basic functionality. If it passes this test, a HASS test as described for the PDBs above is performed as well. After the HASS test, the PDB, MTx, MTRx and fibers are installed on the LTDB. Then, digital functionality and power distribution as well as analog performance are verified, followed by an integration test, all performed using the integration test stand (see Section 5.1), before the LTDB is qualified to be installed on the detector.

Initially, the control links through GBTx as well as the digital readout chain through LOCx2 are verified. Each ASIC, including GBT-SCA, MTRx, MTx, ADC and LOCx2, is configured and checked through the GBT link to verify the control links. The readout chain is verified through ADC test patterns before analog signal injection is exercised. To pass these digital functionality tests, an LTDB must meet the following requirements: slow control, configuration and remote monitoring logic are functioning properly; pedestal tests of the digital readout chains are functioning correctly for all 320 channels; and monitoring information is correct, with the temperature of the digital part at 20 ± 5 °C, the temperature of the analog part at 30 ± 5 °C, and the voltages at their nominal values $\pm 10\%$.

The analog performance integration focuses on the detailed characterization of the full board. Both pedestal tests and pulse tests are performed on the board, as well as tests to measure the signal amplitude and peaking time. Additional testing enables assessment of the INL of each channel while summing testing verifies the summing output and measures the non-linearity of each summing output. All test data and analysis results are examined and logged into a database. To pass these analog functionality tests, an LTDB must meet the following requirements: pedestal tests of analog readout chains are functioning correctly for all 320 channels, with a noise level better than 0.85 of the least significant bit; pulse tests of both analog and digital readout chains are functioning correctly for all 320 channels; the INL is better than 0.35%; all 64 summing channels are functioning correctly; and the power consumption of the whole board is within 95.0 ± 4.5 W.

After the above tests are passed, the cooling interface is installed. Each cooling interface including the cooling blocks and cooling plates is leak-checked in a dedicated test station prior to assembly on the LTDB, and again after installation on the LTDB. If no leak is observed, the boards passing above performance tests are shipped to CERN, where another leak check with pressurized gas is performed in a dedicated test station before installation. Only the boards passing this additional leak check are finally installed on the detector.

3.3.6 Compatibility with Phase-II upgrade

After the Phase-I upgrade and data taking in Run 3, the LTDB boards will still be used in the Phase-II upgrade for Run 4 and beyond as part of a level-0 trigger system [36]. To fully exploit the functionalities of the LTDB in the Phase-II configuration of the LAr trigger and readout system, some design work is needed on the side of the future FEBs. Correct matching between the analog dynamic range of the differential trigger sums that will be provided by the Front-End preamplifier/shaper ASICs and the single-ended analog dynamic range of the LTDB inputs has to be ensured. These design aspects will not be covered here, since

the Phase-II FEBs are currently under development and the details of how to ensure compatibility are not yet fully defined.

On the LTDB side, it is critical to ensure easy adaptation to the configuration of the LAr Front-End system during Phase-II. Seen from the LTDB side, the main differences between Phase-I and Phase-II configurations are:

- In Phase-II, the legacy analog trigger system, based on the analog TBB, will have been decommissioned. The consequence for the LTDB is that the adders that are present to sum groups of four channels will no longer be needed. On the LTDB, these adders build the analog layer sum signals needed by the TBB from the Super Cell signals.
- The PDB will have to be redesigned to adapt to the Phase-II power rail configuration which will provide only one single positive voltage; negative power supply rails will no longer be available. The absence of negative voltages means that it will not be possible anymore to power the (then no longer needed) legacy analog adders. Appropriate measures have been taken so that this situation does not degrade the performance on the Super Cell signal path.

Figure 18 shows a simplified schematic of the LTDB analog adder circuitry. The Super Cell signals are modelled as a voltage source in series with a $50\ \Omega$ resistor. It can be seen that each of the four Super Cells (SC1 to SC4 in Figure 18) that are summed by the legacy adders are connected through a $3.75\ \text{k}\Omega$ resistor to the inverting input of the first of the two inverting amplifiers (AD8001) that make up the complete adder. As long as this amplifier is powered on, its negative input is a virtual ground, and there is no induced crosstalk between Super Cells. On the other hand, once the amplifier is powered off, the Super Cells that are summed together are connected through a resistive network that introduces some resistive crosstalk. Consequently, the resistor values have been chosen high enough to keep the crosstalk below 0.2% . Taking into account the actual resistor values used, the crosstalk between any two Super Cells connected to the same adder is equal to 0.17% . This number has been checked on a test board that has been built for this purpose, featuring a group of four Super Cells and their adder, with the possibility to power off specifically the adder circuit. This shows that the crosstalk induced during Phase-II by the absence of the negative power rail is acceptable.

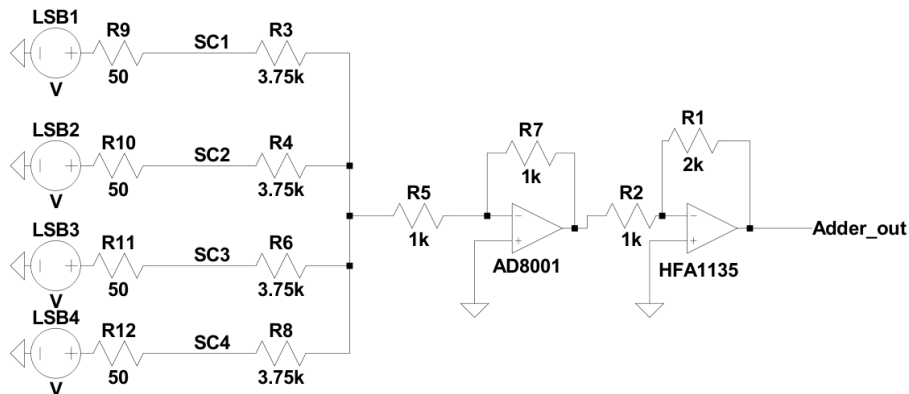


Figure 18: Simplified schematic of the adder implemented on the LTDB for compatibility with the legacy analog trigger system.

4 New Back-End electronics

4.1 LAr carrier

The LAr carrier (LArC) is an ATCA standard cut-out blade with a Rear Transition Module (RTM). The LArC hosts the LATOME processor daughtercards (Section 4.2), sends and receives data from the read out system, and distributes clocks and trigger signals synchronized to the LHC beam clock. Data connectivity includes the ATLAS Trigger and Data Acquisition (TDAQ) system for the global monitoring and standard Ethernet 1 GbE and 10 GbE links. The latter are based on the 10 Gigabit Attachment Unit Interface (XAUI). A photograph of the LArC is shown in Figure 19.

Data are received and/or transmitted on the LArC using five paths: (1) serial Multi-Gigabit Transceiver (MGT) connections of 9.6 Gbps between the LArC and LATOME cards for readout of data on L1A (TDAQ path), (2) readout of 10 Gbps local monitoring data between the LArC and LATOME cards upon user request (local monitoring path), (3) Low Voltage Differential Signaling (LVDS) connections between the carrier and LATOME cards used for clock and trigger distribution, (4) serial transceiver links to optical fibers connected to Small Form-factor Pluggable (SFP+) modules³ on the RTM which provide the external connection for the TDAQ path and (5) serial transceiver links between the carrier and other ATCA boards using the ATCA shelf backplane which provide the external connection for the local monitoring path. The

³ SFP+ modules are an industry standard hot-swappable electro-optical converter module.

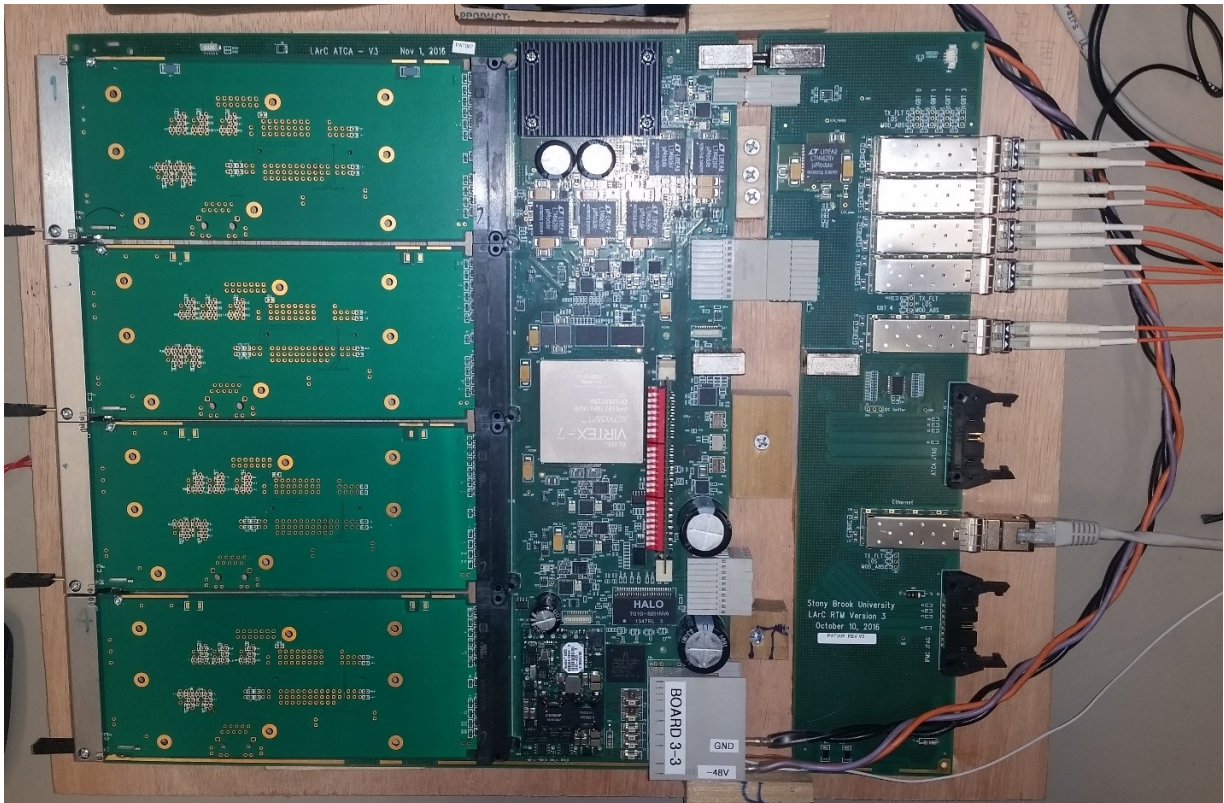


Figure 19: A photograph of the LArC and RTM, with the LArC side panels removed for clarity and testing cards in the AMC sites.

master clock signal and trigger data are recovered from a dedicated link of the TDAQ data path from the ATLAS trigger distribution system to the LArC and distributed to all of the LATOMES.

A block diagram of the carrier data and clock connectivity is shown in Figure 20. The main component on the board is a Xilinx® Virtex®-7 FPGA, part number XC7VX550T-FFG1927-2-E, through which all of the TDAQ and local monitoring data passes. The FPGA boots from onboard flash and has 256 MB of external DDR3 memory. There are four clock domains on the LArC for the TDAQ path, the local monitoring path, the 1 GbE path and a system clock. The TDAQ clock is recovered from the LHC master clock and provides all trigger-related timing.

Along with the dedicated purpose TDAQ and local monitoring links, the carrier provides GbE connections. All GbE links are routed through a BROADCOM switch on the LArC. The GbE links are connected from the switch to the LArC FPGA, each of the 4 LATOME sites, the IPMC module (at 100 Mbps), an SFP cage on the RTM and 2 GbE connections to the ATCA shelf backplane. The redundant backplane connections are required by the ATCA standard.

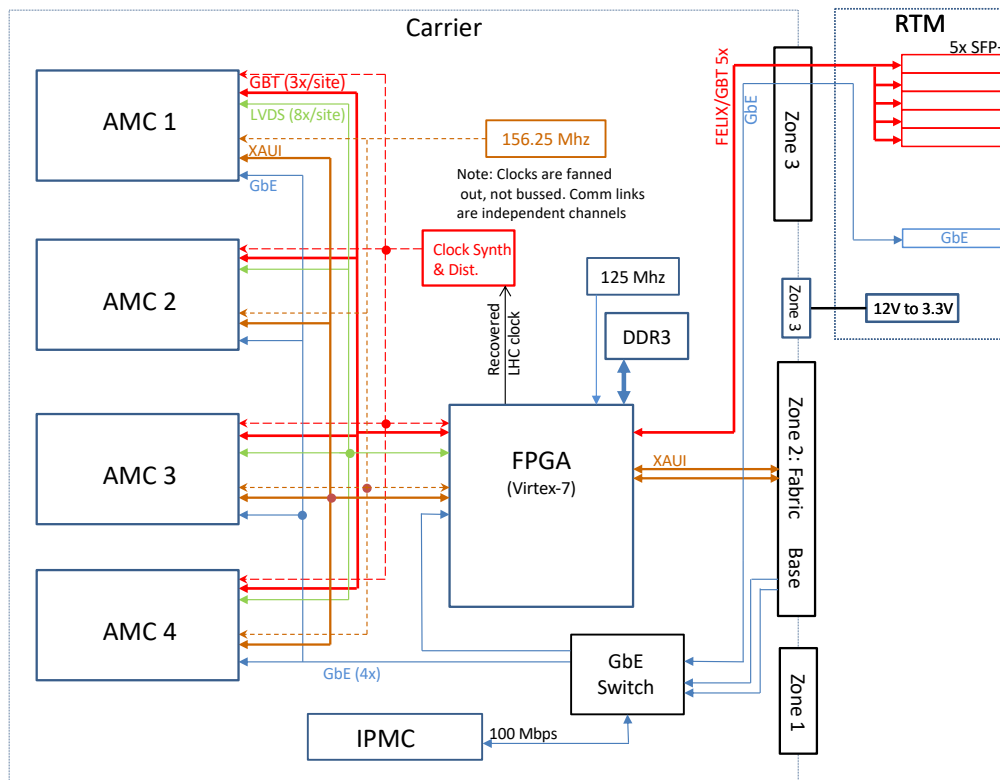


Figure 20: A block diagram of the data and clock connections on the LArC. The GbE connectivity is provided using a BROADCOM BCM5396. The switch is automatically initialized at power on without programming. The switch to the AMC, switch to FPGA and switch to RTM SFP connections are standard 1000Base-X connections. The connections between the switch and the Zone 2 base layer are 1000Base-TX as required by the ATCA standard, and the connections between the switch and the IPMC are 100 Mbps PHY-based links. All XAUI and TDAQ connections are routed through the FPGA. I²C based monitoring and configuration connections are not shown.

The LArC uses an ATLAS standard IPMC (Section 4.3) to provide all board power and sensor management functions. The ATCA standard also specifies electrostatic shielding and status Light Emitting Diodes (LEDs) all of which are included in the carrier. The FPGA can be rebooted without a LArC or shelf power cycle by using dedicated commands sent to the IPMC over the 1 GbE network.

The RTM is used to provide connectivity for 5 TDAQ channels via SFP+ modules. It also has Joint Test Action Group (JTAG) connectors on the back panel providing access to the onboard JTAG chain and an IPMC JTAG interface. An insertion indicator switch is integrated into the RTM insertion/removal handle, and by sensing the switch, RTM power is controlled by user code in the IPMC. This allows hot swapping control of the RTM DC-to-DC converter. The RTM data connection to the carrier is a standard ATCA connector located in carrier zone 3. A second zone 3 connector provides 3.3 V management power and 12 V payload power to the RTM.

The production LArC's and RTM's undergo multistep testing. The first step involves checking the power systems, including a simple resistance test before initial powering on. The second step then tests the infrastructure including JTAG, I2C, IPMC, DDR3, clock generation, and the 1 GbE infrastructure. The next step is testing of all transceiver TDAQ and local monitoring links to 10^{14} and 10^{12} bits respectively, using the industry standard PRBS31 (PseudoRandom Binary Sequence of length $2^{31} - 1$). The LVDS links are also tested at 160 MHz using PRBS31. The tests for the links which connect to LATOME's use special passive loopback cards inserted in the AMC slots during this check. In the final step a boot flash memory is programmed with low-level board management code, and the one-time-programmable FPGA identification eFuse is set. At this point all components and functionality are verified, and the carriers are ready to have LATOMEs installed.

4.2 LAr trigger processing mezzanine

The LATOME board reads incoming data from 48 optical links, processes these data in a high-performance FPGA and sends the results to 48 optical links. The board is also interlinked to the standard Ethernet networks (1 GbE and 10 GbE) and the specific ATLAS network (TDAQ) for monitoring and control purposes. This board fulfills the AMC standard and is plugged into the LArC which provides connectivity as discussed above. Figure 21 shows the LATOME equipped with optical fibers: the black front panel connectors gather the 48 transmitting fibers and the blue ones the 48 receiving fibers. The FPGA and the optical transceivers are cooled down with large copper heatsinks.

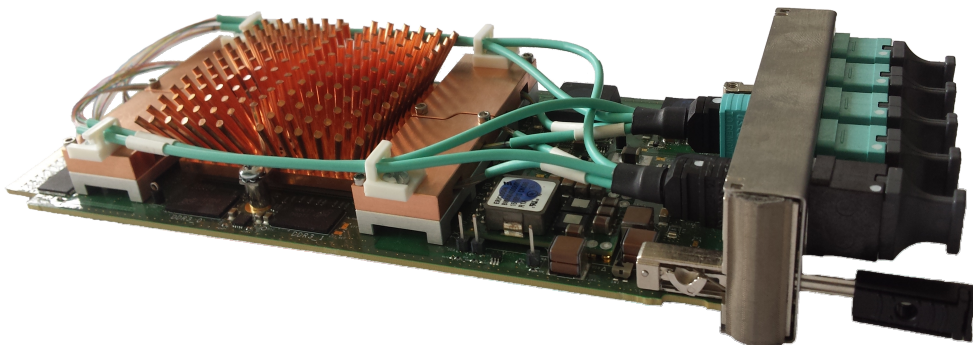


Figure 21: LATOME board equipped with optical fibers.

The board receives LTDB data at 5.12 Gbps and transmits new FEX system data at 11.2 Gbps through four twelve-channel BROADCOM MicroPOD™ receivers and four twelve-channel BROADCOM MicroPOD™ transmitters. These MicroPOD™ modules make the optical to electrical and the electrical to optical conversion for the 2×48 FPGA high speed links. All these links can be synchronized either by a local oscillator with a fixed frequency of 160.316 MHz or by the external clock provided by the LArC. The links to the standard Ethernet (1 GbE and 10 GbE) and the TDAQ (9.6 Gbps) networks are routed through the AMC connector. This connector carries also the common TTC commands over four LVDS links.

On the board, the main component is the Intel® Arria® 10 FPGA, part number 10AX115R3F40E2SG (Figure 22). Four DC/DC converters provide the different voltage supplies to this FPGA. They are enabled by a sequencer chip in order to generate the power on and off sequence required by the Arria® 10. This sequence is triggered by the Modular Management Controller (MMC) chip which manages the AMC hotswap, the onboard sensors (temperature, voltage and current) and the IPMC connection (see Section 4.3 for the IPMC description).

The FPGA firmware boots from a 1 Gb serial flash memory. Two 2 Gb DDR3 external memories are also available to exchange data with the FPGA. Four oscillators (125/156.25/160.316 and 100 MHz) provide all the clocks needed to synchronize the internal FPGA logic.

The LTDB and FEX optical cables are plugged into the LATOME front panel through high density Multi-fiber Push On (MPO) optical connectors. On this front panel there is also access to the FPGA JTAG and test outputs and the MMC JTAG port with external connectors. A reset push button and status LEDs are available as well.

There are two types of LATOME according to the combination of input channels on the MPO connectors and pigtail fibers to the MicroPOD™ modules. The standard LATOME has four MPO connectors of 12 channels (MPO12) while the special LATOME has two MPO connectors of 24 channels (MPO24) and one MPO12 for data reception (Rx). Both LATOME types have one MPO connector of 48 channels for data transmission (Tx).

The LATOME boards were validated after their production in several stages. Once the LATOME is received from the assembly house, the board is stamped with its unique identifier by setting a ten-bit vector with pull down resistors connected to the FPGA input pins. This identifier is used to track the board all along the process. The first stage of validation consists of checking the powering sequence. The board is powered on and the power-up sequence and the DC/DC converters' voltage values are checked. Then the FPGA JTAG connection is verified and all the ports and components interlinked to the FPGA are sequentially tested: oscillators, DDR3, flash memory and ATCA carrier links up to 10^{13} bits with PRBS31 vectors.

Once all the FPGA interfaces are validated, the MMC access to the DC/DC voltage and current values and the FPGA temperature is tested in a stand-alone setup and on an ATCA carrier board to verify the IPMC communication. The final step is to mount all the MicroPOD™ modules and the optical pigtails on the board. An optical loopback is plugged into the front panel to check all the optical links at 11.2 Gbps up to 10^{13} bits with PRBS31 for approximately 15 minutes. At this stage all the components and links of the board are fully validated.

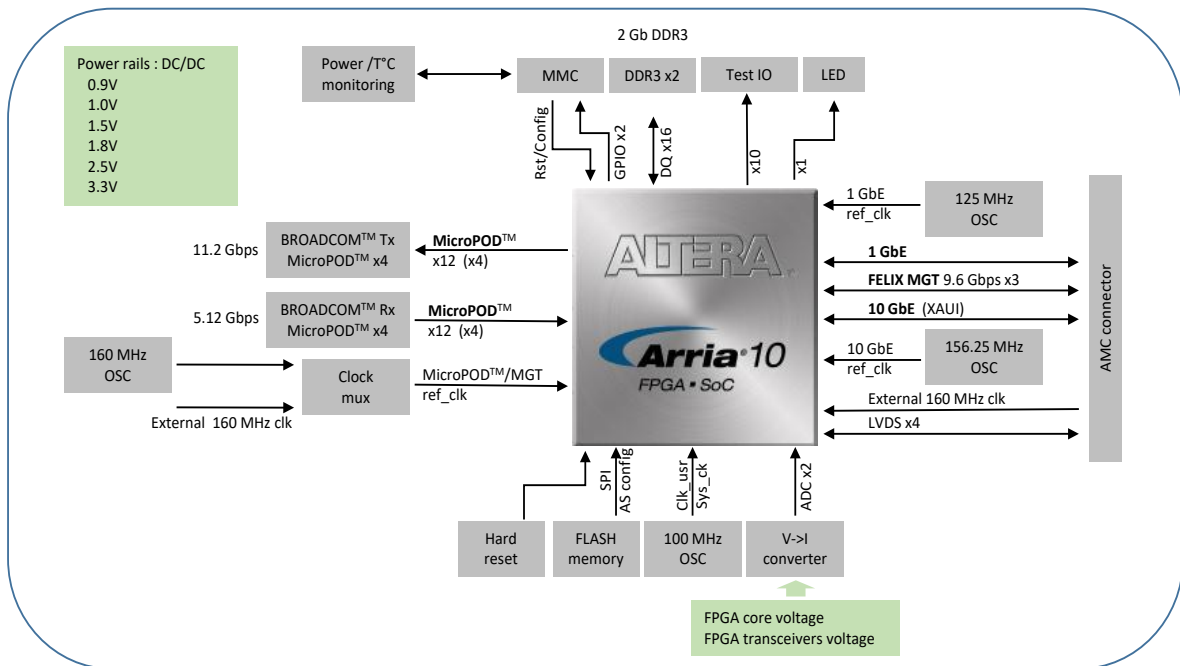


Figure 22: Block diagram of the LATOME board.

4.3 Intelligent platform management controller

The IPMC supports an intelligent hardware management system for ATCA boards and ATCA carrier boards (see Figure 23) which provides the ability to manage the power, cooling, and interconnect needs of intelligent devices: monitoring of events created by electronic on-board devices, logging of such events to a central repository and management of the mezzanine modules according to user's implementation, as well as the communication with the Shelf Manager. Figure 23 presents a photograph of the IPMC in its mini Dual In-line Memory Module (mini-DIMM) form factor accompanied by the functions of the main elements of the board. In addition the IPMC mezzanine, via local IPMB, communicates with the MMC installed on the LATOME AMC. The dimensions of the IPMC mezzanine are $82 \times 17.9 \text{ mm}^2$. The board is equipped with two microcontrollers called IPMC and IOIF (for Input/Output interface) that can be seen on Figure 23. The IPMC controller controls and monitor the operations and the status of the ATCA carrier board, while the IOIF controller provides an extended I/O interface and deals with the non-IPMC features. The main ATCA functions are fulfilled via IPMC, the master board management controller: it controls the AMC and RTM power and monitors the ATCA power. The IOIF, the slave board management controller, ensures dialog with the sensors located on the carrier. The microcontrollers are loaded with the IPMC software, based on Intelligent platform management Controller software (ICARE) framework [37] which is fully compliant with the ATCA specifications⁴. ICARE is an open-source software which manages ATCA requirements, provides features to build user code and tools to generate some Field Replaceable Units (FRU) and Sensor Data Records (SDR). ICARE provides command line and remote command lines interpretation, acts as the firmware upgrade server and Transmission Control Protocol (TCP) and User Datagram Protocol (UDP) echo server. In addition it provides a Xilinx® Virtual Cable server.

⁴ IPMI v1.5 (document revision 1.1) and some relevant subset of IPMI v2.0 (document revision 1.0); PICMG 3.0 R3.0 (AdvancedTCA™ base specification) and AMC.0 R2.0 (AdvancedMC™ base specification).

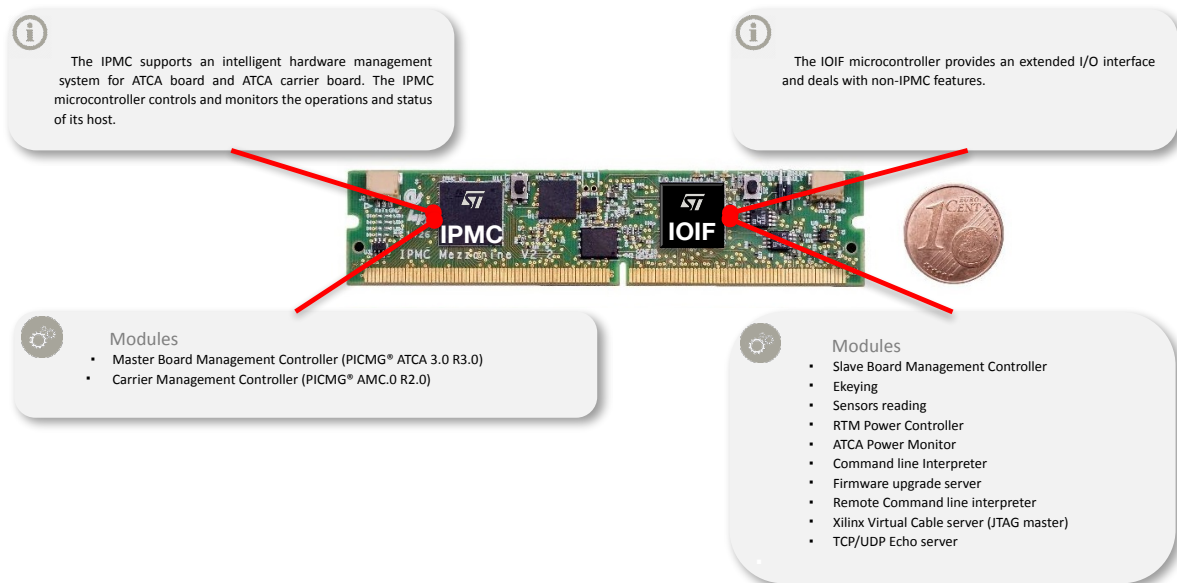


Figure 23: A photograph of the IPMC board, with diagrams detailing the functions of each microcontroller.

4.4 Back-End firmware

4.4.1 LAr carrier firmware

The primary tasks of the LArC firmware are to provide TTC clock and TTC event information to the LATOMEs and to transmit data from the LATOMEs to downstream consumers such as FELIX or LAr Monitoring PCs. The FPGA firmware is developed using the Xilinx® Vivado IDE including SDK for MicroBlaze applications.

A simplified block diagram of the firmware is shown in Figure 24. The firmware framework uses a MicroBlaze processor as an embedded system and lightweight IP (lwIP) for network connectivity. The system clock is a crystal-generated 125 MHz.

The main functionalities of the LArC firmware are described in the following paragraphs.

GbE Communication GbE is connected to the FPGA via a Broadcom GbE switch on the LArC. This switch is also connected to the Zone 2 Base Interface of the ATCA shelf. Ethernet connectivity is implemented using the lwIP software running on the MicroBlaze processor. GbE data are received and transmitted as Ethernet packets. The protocol used is either raw UDP packets or IPbus [38] packets embedded in the UDP packets. The latter is used in normal operation while the former is useful for sanity tests. The two protocols are assigned different ports in the LArC software. The handling of these protocols is done through C code running on the MicroBlaze processor.

I²C Communication There are two I²C buses on the LArC. One is mastered by the IPMC and includes a sensor bus connection to the FPGA in the chain. The other connects the FPGA with the clock generators

packet enters a Xilinx[®] multiplexer IP. This multiplexer receives packets from the four 10 GbE MACs using a round-robin algorithm and sends them to a bidirectional switch engine connected to a Xilinx[®] demultiplexer IP. This demultiplexer sends packets to 10 GbE output MACs. MAC and XAUI IP cores are used to send the switch output to the Zone 2 Fabric Interface. The transmitted data can be standard or jumbo UDP packets. The current maximum size of the packet is 16 384 bytes, which matches the capabilities of the network switch residing in the ATCA shelf.

MGT Data Transmission Four sets of MGT serial lines between the RTM and LArC FPGA are used to carry LATOME data to be recorded by ATLAS via the FELIX system. These data are sent on receipt of an L1A. The bandwidth is 9.6 Gbps in Full Mode [11] data format. It is essentially 8b/10b encoded but with additional control specifications for start and end of the packet and BUSY. TDAQ stream data are transmitted from each LATOME to the LArC. The data are received and deserialized on one transceiver pair and subsequently serialized and transmitted on a second transceiver pair. The data are transmitted to optical modules on the RTM and then to FELIX. Plain Xilinx[®] GTH transceiver IP is used for transceiver instantiation in the firmware.

Resource Usage The resource usage with a current LArC project is shown in Table 3 and comfortably fits in the device.

Table 3: Resource utilization in the LArC firmware project. Each memory block corresponds to 36 Kbits of data.

Resource	Used blocks	Utilization [%]
Logic	138343	11.4
Memory	452	38.3
DSP	5	0.2
Pins	128	21.3
Gigabit Transceivers	34	42.5
Global Clock Buffers	29	90.6
Clock Managers	6	15.0

Validation and verification A limited number of logic modules were simulated via Questa[®] from Mentor Graphics[®] and Xcelium[®] from Cadence[®]. A dedicated validation procedure was used to generate and check the expected data. In general, Vivado projects for individual modules were developed and tested on the LArC hardware using the Xilinx[®] Integrated Logic Analyzer (ILA). The individual modules were subsequently integrated into a complete project. The complete project was tested using a LArC, a number of LATOME modules, and external connections to FELIX and monitoring PCs. In this case the integrity of the project was validated by testing carried out at CERN and other laboratories. The tests involved stimulation by known inputs and comparison between actual and expected outputs.

4.4.2 LAr trigger processing mezzanine firmware

The LATOME firmware performs four main functions:

- Handling of up to 48 high speed input links from one or more LTDBs, corresponding to up to 320 Super Cells
- Application of a digital filtering algorithm to reconstruct the Super Cell transverse energy every 25 ns and to identify the bunch crossing when the deposited energy was initiated (BCID determination)
- Outputs results every 25 ns to the Level-1 calorimeter trigger system (FEX)
- Processes and buffers data to be delivered to the TDAQ readout chain and to the local monitoring, upon request (L1A or other)

The FPGA processing of the 40 MHz path from the LTDBs and directed to the FEX system has to be performed with a fixed latency, in order to correctly work within the ATLAS trigger readout system. This processing is divided in several steps. First, the incoming LTDB data are deserialized and descrambled. The 12-bit ADC data at 40 MHz for each channel are aligned accordingly in preparation for the application of the filtering algorithm. Next, to ease the computations made by the FEX system later on, data words are organized following the detector geometry in a configurable way. The Super Cell transverse energies are then calculated with filtering algorithms. Finally, the transverse energies are encoded without losing the benefit of the LAr fine energy granularity for cluster reconstruction in the FEX system. An important point to be considered is the case of saturated inputs which have different shapes than nominal pulses and for which the BCID determination may fail. The correct bunch crossing has to be identified with a dedicated filter on the signal in this case. The implementation of these steps in the LATOME firmware design is detailed in the following paragraphs.

Figure 25 presents a block diagram of the LATOME firmware. The firmware is built around the Low-Level Interface (LLI) which controls the hardware components of the LATOME. The firmware consists of a main data path (from LTDB to FEX) which has been organized in four blocks, input stage (IS), configurable remapping (CR), user code (UC) and output summing (OS). Three other functions are included in the firmware: (1) TDAQ/monitoring (MON) which organizes the transfer of data to TDAQ and to the local monitoring processes, (2) the IPbus [38] controller (IPCTRL) which is the interface for the LATOME slow-control system and (3) the TTC which decodes and provides signals from the TTC system.

Figure 26 presents a block diagram of the various clocks organisation inside the LATOME firmware. Three major clock domains are defined. A 320 MHz clock is used from the input LTDB to the configurable remapping. The configurable remapping transfers data to the user code, which receives, computes and transmits, at the frequency of 240 MHz. The clock frequency is reduced to ease the routing and timing of the signals. This increases the size of the logic needed since it needs to go from 48 input streams to 62 streams at the user code level. The output summing transfers FEX data at 280 MHz. This frequency is required to handle the output data protocol at 11.2 Gbps, comprising 7 LHC cycles per data frame (one LHC cycle corresponds to 40 MHz).

The latencies of each processing step have been estimated by simulations and then confirmed by measurements in the system as-built. The measured latencies are listed in Table 6 in Section 5.4. From the reception of the data to their transmission to the FEX system, the LATOME firmware latency is approximately 16.6 LHC clock cycles. In the following, the different firmware blocks are briefly detailed.

Low-Level Interface The LLI implements all the FPGA device specific IPs configured in the Quartus® tool from Intel®. The aim of the LLI is to have device agnostic interfaces between the inputs/outputs of the FPGA and the internal blocks. This is most commonly known as board support package (BSP). All the

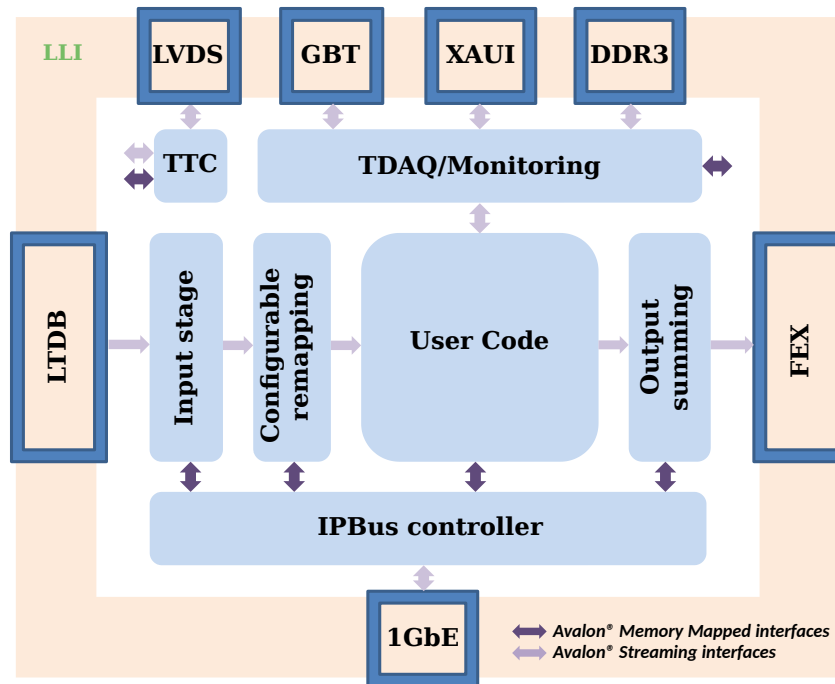


Figure 25: LATOME firmware block diagram. The pale brown frame corresponds to the interface with the hardware while the blue boxes correspond to the higher level functional blocks.

interfaces between the LLI and the FPGA core layers are designed with standard Avalon Streaming and Avalon Memory Mapped interfaces [39]. This allows for well-defined and documented standard interfaces between each one of the blocks.

The LLI implements the following IP blocks:

- Clock PLLs and synchronous resets for all various clock domains
- Flash interface for remote programming
- Gigabit Ethernet for slow control
- 4 LVDS lines at 160 MHz for TTC data input
- 48 5.12 Gbps transceivers for LTDB inputs
- 48 11.2 Gbps transceivers for FEX outputs
- XAUI 10 Gbps ethernet (10 GbE) for local monitoring output
- DDR3 interface for local memory

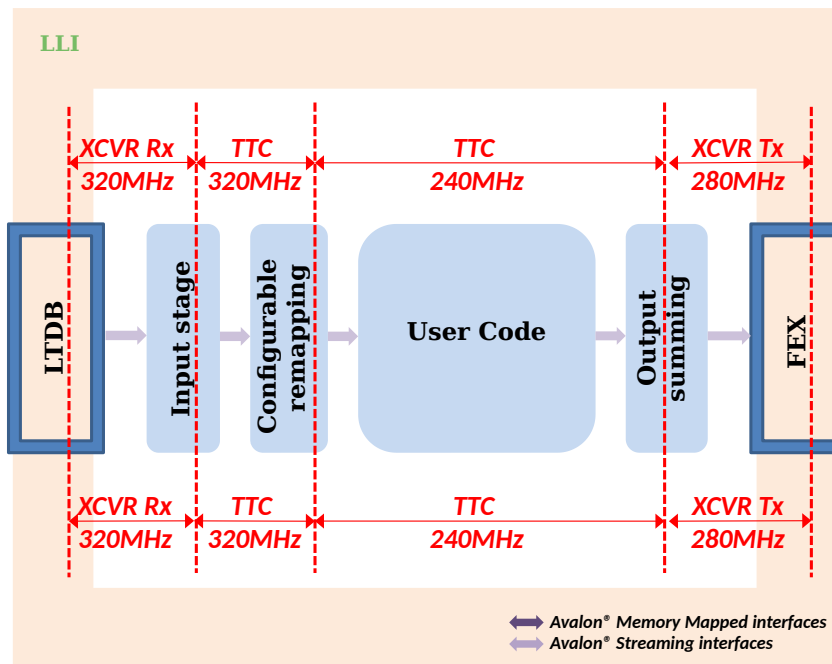


Figure 26: LATOME firmware clock domains block diagram. The reference clocks are taken either from the transceivers (XCVR) connected to the LTDBs or the FEX system, or from the LHC reference clock provided by the TTC block.

Input Stage The LTDB data are sent to the LATOME on optical fibers that carry the data stream at 5.12 Gbps using the LOCic protocol [40]. The role of the input stage is to decode this protocol and align all input streams to the same BCID. It is split into three parts:

- Reception and processing of the LTDB data streams where decoding of LOCic protocol is handled
- Fiber to fiber alignment where all input streams are aligned to the same BCID
- Test pattern generator which can be used internally to generate test data

Configurable Remapping The configurable remapping block is used to reorder data coming from the input stage following the detector geometry for each bunch crossing. This block groups data from Super Cells belonging to the same Trigger Tower and then sends them to one of the User Code block instances. This prepares data for some part of the FEX system where the unit is a Trigger Tower. As the data arrangement and the geometry are not uniform across the detector and are therefore different for each LATOME, the block is configured specifically at startup.

User Code The User Code block receives the Super Cell data from the Configurable Remapping block and outputs synchronously the reconstructed transverse energy and data quality bits to the Output Summing block, at the corresponding bunch crossing with a fixed latency. The different operations implemented in the User Code module are illustrated in Figure 27.

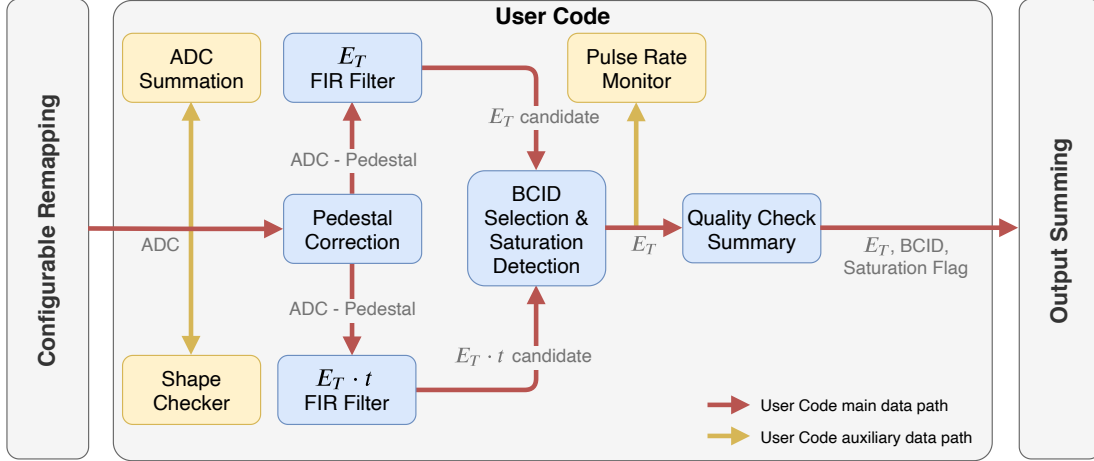


Figure 27: Block diagram of the User Code module in the LATOME firmware. The red arrows represent the data flow corresponding to the digital trigger readout, while the yellow arrows represent auxiliary paths used for basic tests (more details in the text).

First, a BCID-dependent pedestal correction is applied to the Super Cell ADC value, in order to take into account the imperfect pile-up effect cancellation with the bipolar pulse shape from events occurring at the beginning of an LHC bunch train: With long trains and for distances from the beginning of the trains smaller than the typical drift time in LAr gaps (450 ns in the EM barrel calorimeter, less in the FCAL) an average positive energy shift from pile-up is expected, as the contributions from out-of-time pile-up does not cancel the in-time pile-up contribution. After 20 BCIDs (500 ns) the average shift is alleviated thanks to the bipolar shaping applied in the readout, since the total contribution from out-of-time pile-up compensates here for the in-time pile-up contribution. This BCID-dependent pedestal correction depends on the LHC bunch scheme, the instantaneous luminosity of each bunch and the pulse shape of each Super Cell. Consequently, the correction is computed directly on the LATOME FPGA for every BC position and for every Super Cell and updated approximately every 10 seconds with a round-robin scheme. It is calculated from Super Cell ADC counts averaged over 1024 LHC cycles, processing only 156 BC positions at a time, with a 1/8 ADC count precision and a maximal absolute value of 32 ADC counts. Two Finite Impulse Response (FIR) filters, based on an optimal filtering algorithm [41], then compute the E_T and the product of E_T and time ($E_T \cdot t$) from a fixed number of ADC input values (four in the actual implementation). The coefficients used in the optimal filtering algorithm include a geometrical factor to compute directly the E_T from the ADC values rather than the Super Cell energy. From the E_T and $E_T \cdot t$ candidate values computed every bunch crossing a BCID selection algorithm determines the correct E_T and BCID of the Super Cell signal. The E_T and BCID are considered correct if at a given BCID b the following condition is fulfilled:

$$\begin{cases} 8E_T(b) < E_T \cdot t(b) < -8E_T(b), & \text{if } -1 < E_T(b) \leq 0 \text{ GeV} \\ -8E_T(b) < E_T \cdot t(b) < 8E_T(b), & \text{if } 0 < E_T(b) \leq 10 \text{ GeV} \\ -8E_T(b) < E_T \cdot t(b) < 16E_T(b), & \text{if } E_T(b) > 10 \text{ GeV}. \end{cases} \quad (1)$$

The threshold values utilize powers of two to ease the FPGA computation. Because of resolution effects,

some thresholds are negative ($-8E_T$). For E_T values above 10 GeV the selection window is asymmetric, with a looser boundary towards high $E_T \cdot t$ values, to avoid wrong BCID assignments to delayed signals coming from hypothetical long-lived particles.

In the case of saturated inputs, the proper bunch crossing is identified with a dedicated selection criterion based on the expected shape deformation and a flag is raised on the passed data. Figure 28 shows the $E_T \cdot t$ as a function of E_T measured in calibration runs with injected signals of known E_T and bunch crossing (BC), for some middle layer Super Cells in the EMB calorimeter. Values are either computed with the four ADC inputs leading to a correct BCID assignment (circles) or with four ADC inputs in neighboring time windows leading to incorrect BCID assignments of +1, -1 or -2 BC (triangles and squares). The BCID selection criterion of Equation (1) is represented in the figure by the triangular green shaded area. The data correspond to special calibration runs with injected E_T values spanning the linear and saturated regimes. The saturation effect can be observed with the $E_T \cdot t$ versus E_T dependence becoming non-linear at high E_T values. In this case, $E_T \cdot t$ is biased towards lower values because the saturated pulses have a shorter rise time.

The saturation flag is raised in case the E_T and $E_T \cdot t$ candidate values for the two consecutive BCIDs $b - 1$ and b follow simultaneously the conditions

$$\begin{cases} E_T(b-1) > E_T^{\min \text{ previous}} & \text{and } \xi^{\min \text{ previous}} < E_T \cdot t(b-1) < \xi^{\max \text{ previous}} \\ E_T(b) > E_T^{\min} & \text{and } \xi^{\min} < E_T \cdot t(b) < \xi^{\max}, \end{cases} \quad (2)$$

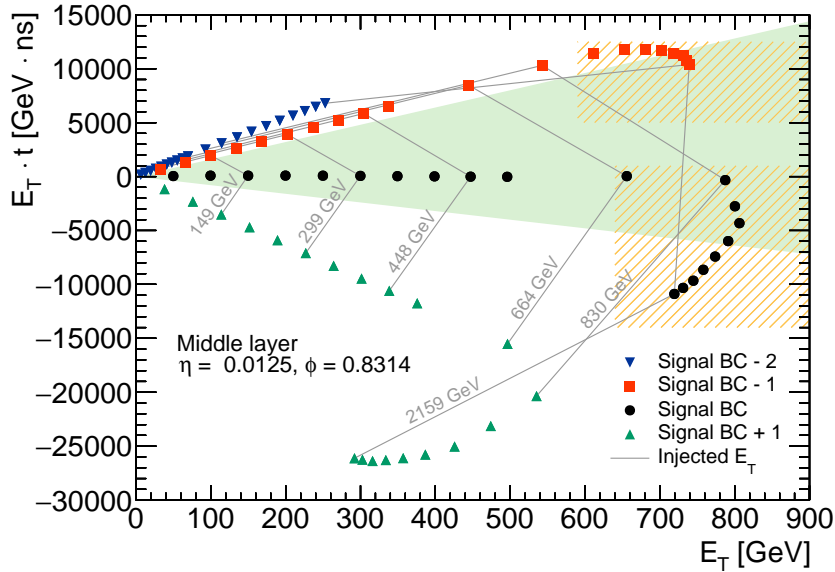


Figure 28: $E_T \cdot t$ as a function of E_T measured in calibration runs with injected signals of known E_T and bunch crossing. Values are either computed with the four ADC inputs leading to a correct BCID assignment (Signal BC) or with four ADC inputs in neighboring time windows leading to incorrect BCID assignments of +1, -1 or -2 BC (Signal BC ± 1 or -2). For some injected E_T values, grey contours link the $(E_T, E_T \cdot t)$ points measured from the same injected signal but with ADC inputs from different time windows. The green shaded area corresponds to the BCID selection criterion in the case of non-saturated inputs. The orange hatched areas represent the saturation detection conditions. The data correspond to the middle layer Super Cells in the $\eta = 0.0125$ and $\phi = 0.8314$ calorimeter region, where saturation occurs approximately above 750 GeV.

where $E_T^{\min \text{ previous}}$, E_T^{\min} and $\xi^{\min \text{ previous}}$, ξ^{\min} are configurable thresholds on E_T and $E_T \cdot t$ values for BCID $b - 1$ and b , respectively. These detection criteria correspond to the orange hatched areas in Figure 28. The condition on the previous BCID $b - 1$ could in principle be sufficient to detect the saturation, but enforcing the simultaneous verification on BCID b adds more robustness without degrading the computation time.

Once the BCID selection and saturation detection is completed, the corresponding quality bits are stored into the input of the Output Summing firmware block together with the Super Cell's E_T and BCID. If the BCID selection is fulfilled neither for the regular nor the saturated inputs processing, meaning that no physics signal is present, the E_T result is set to zero. While the ADC values are encoded with 12 bits at the input of the User Code, the calculated E_T at the output is encoded with 18 bits with a precision of 12.5 MeV per least significant bit. This is needed to reach the numerical accuracy required by the FEX system (see the "Output Summing" paragraph).

Three auxiliary functions in the User Code module were developed to ease testing and commissioning of the firmware. The ADC Summation adds the Super Cell ADC values over a period of time corresponding to one LHC orbit (3564 BCs). This helps to quickly check the pedestal values of every channel. The Shape Checker detects if a pulse is observed in a given Super Cell from the ADC values of six consecutive samples. The Pulse Rate Monitor provides a similar functionality, but based on the E_T value computed by the FIR Filter. It measures the number of detected pulses above a configurable E_T threshold. These two submodules are useful to check the hardware connectivity, the channel mapping in the firmware and the time alignment of the measured signals. All of these auxiliary functions are not part of the main data flow and can only be read out via the slow-control interface based on IPbus.

Output Summing The main task of the Output Summing block is to group the data received from the User Code in order to compute the sums over specific $\eta - \phi$ areas and to send the data to the FEX output fibers. The characteristics of these sums are compiled in Table 4. The eFEX system aims for identifying isolated energy deposits indicative of electrons, photons and tau leptons. To achieve an optimal hadronic background rejection with a topological discrimination, the full Super Cell granularity is required: no sum is performed and the E_T of each Super Cell is sent directly. The jFEX system targets jet, large-area tau leptons, missing E_T and total- E_T triggers, while the gFEX system is designed for large-area jets, missing E_T and sum E_T online detection. Consequently, a coarser granularity can be used compared to the eFEX system: for the jFEX (gFEX), Super Cells are summed to provide the E_T of the Trigger (gFEX) Towers, covering 0.1×0.1 (0.2×0.2) $\eta - \phi$ areas in the central part of the detector. In the forward region a coarser granularity is used. In case of the gFEX, a position code is added to the output data to provide some information about the location of the most energetic deposit within the tower. Flags are attached to the output data for the three subsystems to specify if a Super Cell passes the saturation condition or if there was a problem in receiving or calculating the Super Cell's E_T .

The accuracy (number of bits) for each FEX subsystem is adjusted on multi-linear precision plateaus, as described in Table 5, and data are encapsulated with headers and trailers to be sent to the LLI and further to the FEX system. Another task of the block is to duplicate some FEX outputs several times, according to the number of receivers of the data for specific $\eta - \phi$ areas. Because of these duplications, the data flow rate at the output of one LATOME directed to the FEX system (about 350 Gbps) is larger than the data flow rate at the input of one LATOME coming from the LTDBs (about 200 Gbps). Taking into account all LATOMEs, the total data rate sent to the FEX system is slightly above 40 Tbps.

Table 4: Characteristics of the sums made in the Output Summing block for the electromagnetic (eFEX), jet (jFEX) and global (gFEX) feature extractors. The quoted granularity is provided for the central part of the detector; a coarser granularity is used in the forward region.

E_T sum characteristics	eFEX	jFEX	gFEX
$\Delta\eta \times \Delta\phi$ granularity	0.025×0.1 or 0.1×0.1	0.1×0.1	0.2×0.2
Longitudinal granularity	All layers separated	All layers summed together	
Total number of sums	34048	5760	1984

Table 5: Energy precision of the sums made in the Output Summing block depending on the energy range considered for the electromagnetic, jet and global feature extractors.

Energy precision [MeV]	Energy range [MeV]		
	eFEX	jFEX	gFEX
25	[-750, 1600[[-3150, 6400[[-12800, 12800[
50	[1600, 6400[[6400, 25600[[-50000, -12800[\cup [12800, 51200[
100	[6400, 25600[[25600, 102400[[51200, 200000[
200	[25600, 102400[[102400, 409600[–
400	[102400, 200000[[409600, 800000[–
25600	–	–	[200000, 1019200[
102400	[200000, 1019200[–	–
Encoding	10 bits	12 bits	12 bits

TDAQ Readout and Monitoring The TDAQ/Monitoring block takes care of sending data to two external paths upon L1A. This is used for monitoring, debugging and online or offline analysis. ADC data and transverse energy data from each Super Cell are buffered until the arrival of a L1A signal, and then written to the output links via the transceivers in the LArC as discussed in Sections 4.1 and 4.4.1.

Slow Control The slow control interface connects the firmware blocks to the outside world to allow the user to load or change all the configuration parameters of the system. It is also used to monitor its status. The transport mechanism for the slow control interface is the IPbus protocol [38] over Gigabit Ethernet (1 GbE).

TTC The TTC block receives the TTC signals along the LVDS lines, from the LArC board. It takes care of decoding the relevant TTC information to be provided to the other firmware modules. The TTC block communicates with the input stage and TDAQ/Monitoring blocks.

Verification and validation In order to test the firmware, a Python/C model of the firmware has been developed. Several types of data have been defined and are fed to this model which generates expected data

for all stages in the firmware. These datasets are used in multiple simulation testbenches to test all blocks one by one, bit by bit. The same datasets are used to test the functionality on the real hardware using a secondary LATOME that acts as a data generator and also as a data checker.

Simulations and tests on the target are integrated in the GitLab Continuous Integration flow (CI) to be able to detect and track regressions.

5 Integration tests

5.1 Front-End boards integration tests

The LTDB production test stand evolved from initially using analog signal injection boards based on the commercial FPGA and digital-to-analog converter evaluation boards Xilinx[®] ZC706 and TI DAC3484EVM, to their eventual full integration in the Saclay Test Module (STM), as shown in Figure 29 [42]. All test results shown below are obtained with the evaluation-boards-based test stand, where the LAr Super Cell signals are produced on a signal generator board with 320 DAC channels, and then injected to the LTDB. The 64 summing signals from the LTDB are sent back to the injection board for measurement. A FELIX prototype (a PCI-e card) is used to simulate the Back-End electronics to communicate with the LTDB through five control links and up to 40 data links. The control links send the control and timing information to, and collect monitoring information from the LTDB. The data links receive the ADC data from the LTDB.

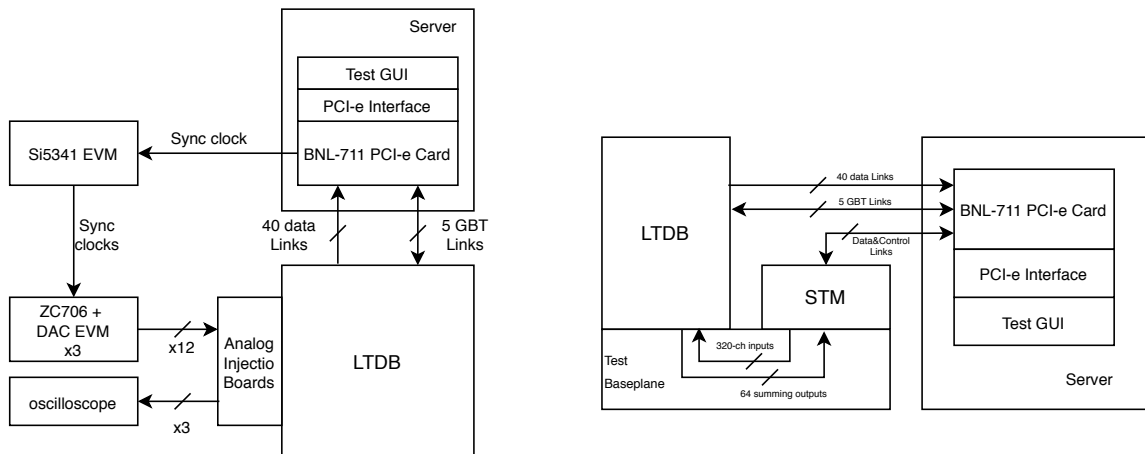


Figure 29: Block diagrams of the LTDB test stands. The left one is the test stand with analog injection boards fed by commercial evaluation boards as signal generator. The outputs of the summing signals are collected and measured on the analog injection boards. The right block diagram illustrates the integrated test stand with STM and test baseplane, where the signals generated on the STM are sent to the LTDB through the test baseplane. Outputs of the summing signals are collected and measured on the STM as well. Both test stands use a FELIX prototype PCI-e card to serve as Back-End electronics for receiving data from the LTDB, timing, control and monitoring.

Pedestals and noise are measured for each LTDB for each channel without any signal injection. The pedestal values then show the electronics baseline level, which simplifies the inspection of the full LTDB for dead channels. The noise distribution of one LTDB board is shown in Figure 30.

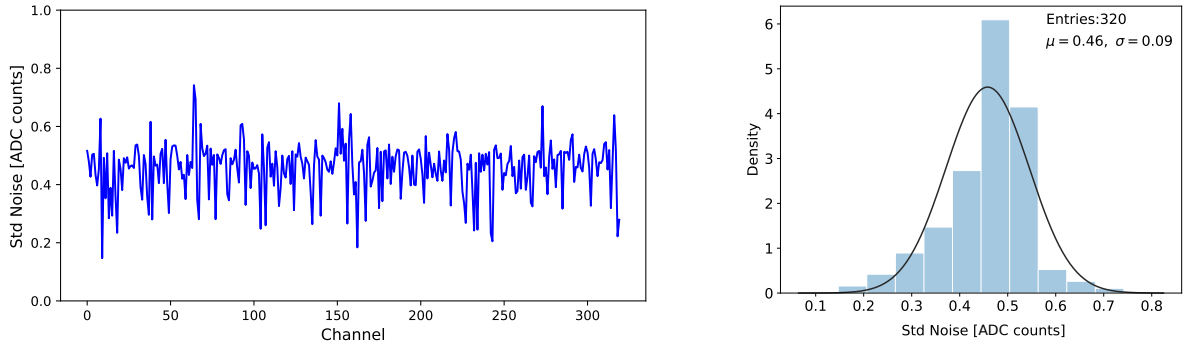


Figure 30: Example noise distribution of an EMB LTDB. The left plot shows the noise of each channel, and the right histogram shows the distribution of the noise values of all the 320 channels with an overlaid Gaussian fit. The average noise is 0.46 ADC counts, which meets the LTDB design requirements.

Simultaneous LAr signals are injected to each LTDB for the integration performance tests. Delay runs are used to measure the amplitude and peaking time of the signals in each channel, using a series of 15 LAr pulses, each delayed by 1.67 ns with respect to the previous. With this method, the reconstruction of the LAr signal pulse has an effective sampling interval of 1.67 ns. An example distribution of amplitude and peaking time is shown in Figures 31 and 32. Ramp runs are used to measure the linearity of each channel, using a series of 16 LAr signals injected with different amplitudes, which are equally spaced from the baseline to the maximum signal close to ADC saturation. An example distribution of the INL is shown in Figure 33.

There are 64 summing output channels per LTDB. The average INL of each channel is around 0.1%, measured with an oscilloscope.

5.2 Back-End boards integration tests

These integration tests are performed on LArC and LATOME assembled together before their installation. There are two types of LATOME according to the combination of input channels on the MPO connectors and pigtail fibers to the microPODs as already discussed in Section 4.2. Up to four LATOMEs of the same type are used to assemble one LDPB. In total 22 (8) standard (special) LDPBs are assembled and tested. Spare LDPBs are validated in the same way.

After further visual inspection⁵ to verify the type of LATOME and the IPMC on the LArC to be mounted properly, the LDPB and the RTM board are plugged into a slot of the ATCA shelf in order to check the ATCA system connectivity:

- The state of the module is checked with LEDs on the front panel. On the ATCA shelf-manager, connectivities to the IPMC on the LArC and MMCs on each LATOME are verified by checking that the topology and the hardware names are correctly recognized.

⁵ Already inspected at production stage, the identification number on the sticker and on the front panel, PCB edge cutting, and holding of heat-sinks are verified once more.

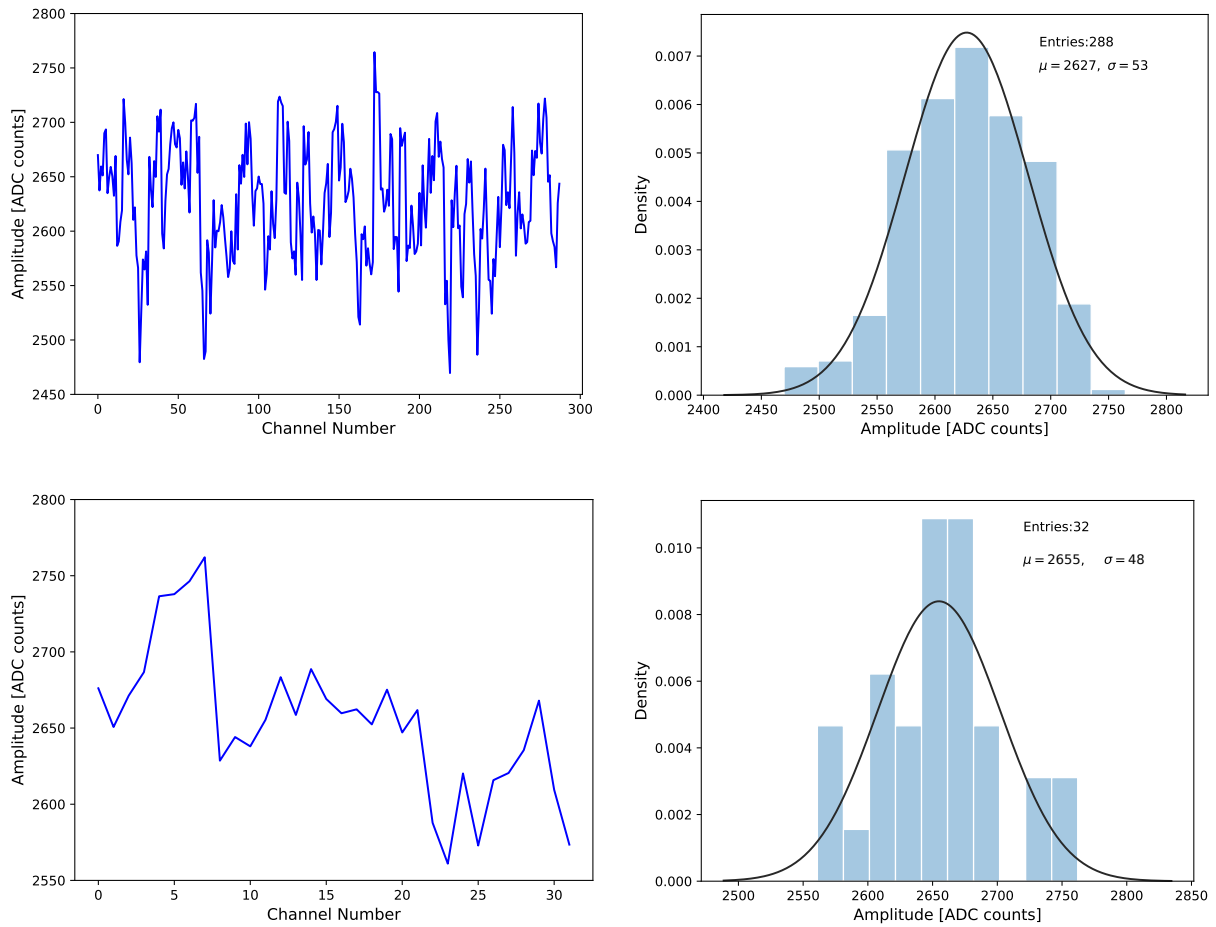


Figure 31: Example amplitude distribution of an EMB LTDB, where a front layer LAr signal with about 1.5 V amplitude is injected into the LTDB. The left plots show the amplitude of each channel, while the right plots show the distribution of the amplitude values with an overlaid Gaussian fit. The top two plots show the amplitude of the 288 50-ohm channels with an average amplitude value of 2627 ADC counts. The bottom two plots show the amplitude of the 32 high-impedance channels with an average amplitude value of 2655 ADC counts.

- A JTAG cable is connected to the RTM in order to verify that the JTAG chain has five FPGAs, four Intel® Arria® 10 FPGAs and one Xilinx® Virtex®-7 with the Quartus and the Vivado software.
- The factory and the application firmware images are loaded to the flash on each LATOME and the following checks are performed: (1) the boot sequence of the factory firmware is verified upon a power cycle of the LATOME, and (2) connectivities to the GbE network are checked with responses of the ping command to IPMC, LArC and all LATOMEs from the PC on the same network.

The next step is an optical data transmission test on the main data path for all links. This is performed with a pair of LATOMEs connected to each other, instead of a simple loop-back, with custom made 48 fiber bundles. These have an MPO48 connector for the LATOME Tx side and four MPO12 (or two MPO24 and one MPO12) connectors for the Rx side. On the LATOME, the application firmware is loaded and configured with a fiber mapping corresponding to the LATOME connector type. On the LArC, the TTC generator is used to provide the 160.2 MHz reference clock and BCR to LATOMEs via an LVDS line.

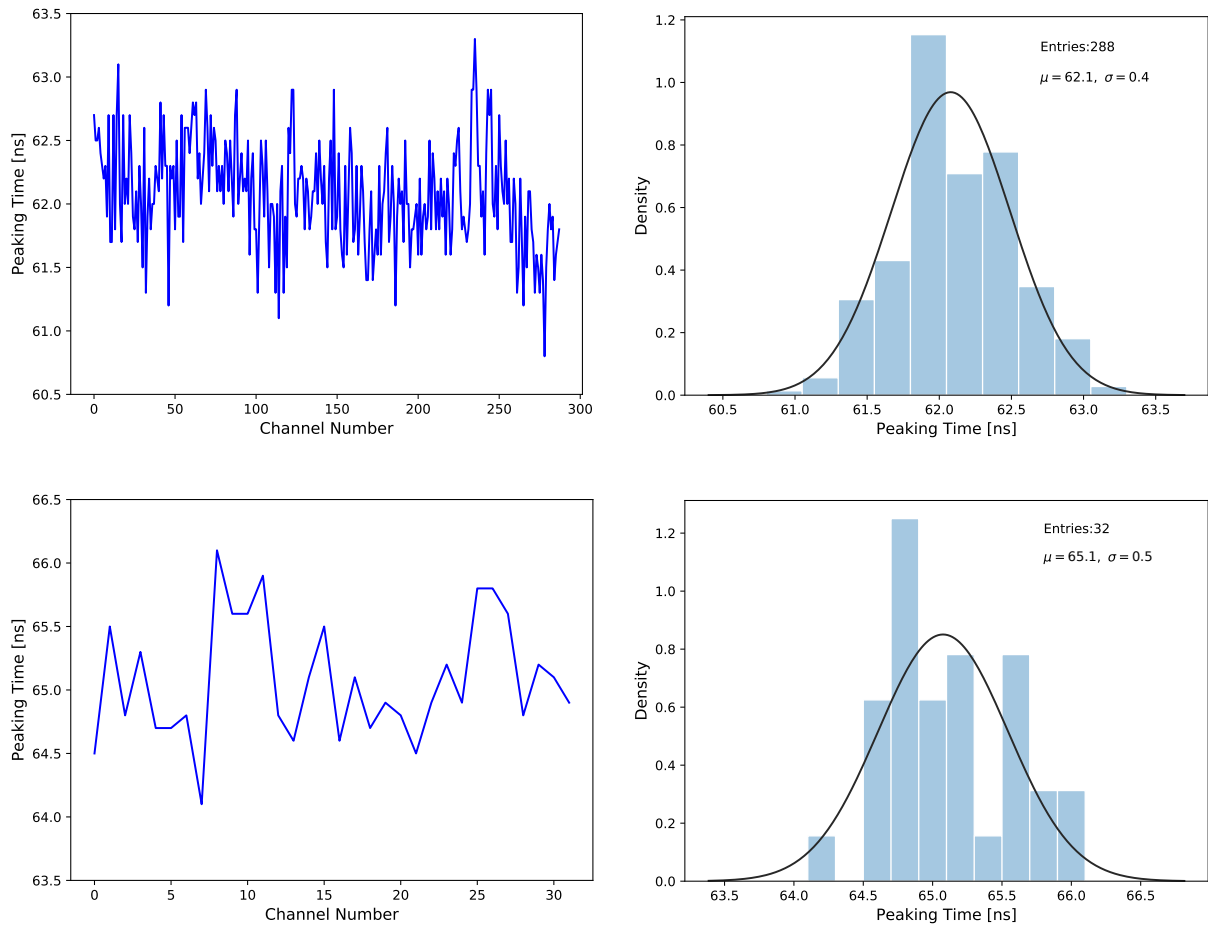


Figure 32: Example peaking time distribution of an EMB LTDB, where a front layer LAr signal with about 1.5 V amplitude is injected into the LTDB. The left plots show the peaking time of each channel, and the right plots show the distribution of the peaking time values with an overlaid Gaussian fit. The top two plots show the peaking time of the 288 50-ohm channels with an average peaking time of 62.1 ns. The bottom two plots show the peaking time of the 32 high-impedance channels with an average peaking time of 65.1 ns.

The synchronization of the LATOMEs with the reference clock is verified, as well as the reception of the BCR with a known period. Then the data transmission test is performed with the PRBS31 data. These procedures certify the stability of clock and BCR reception at the LATOMEs and the main optical data transmission capabilities.

The TDAQ and local monitoring readout paths are both verified by counting the numbers of packets sent from each LATOME and received on the LArC. These numbers are compared to the numbers of trigger signals provided by the TTC generator on the LArC.

The long-term stability is also checked by keeping power up and monitored for one week. All monitoring sensors related to power load and temperatures are read out. After the long-term stability test, all connectivity tests are repeated.

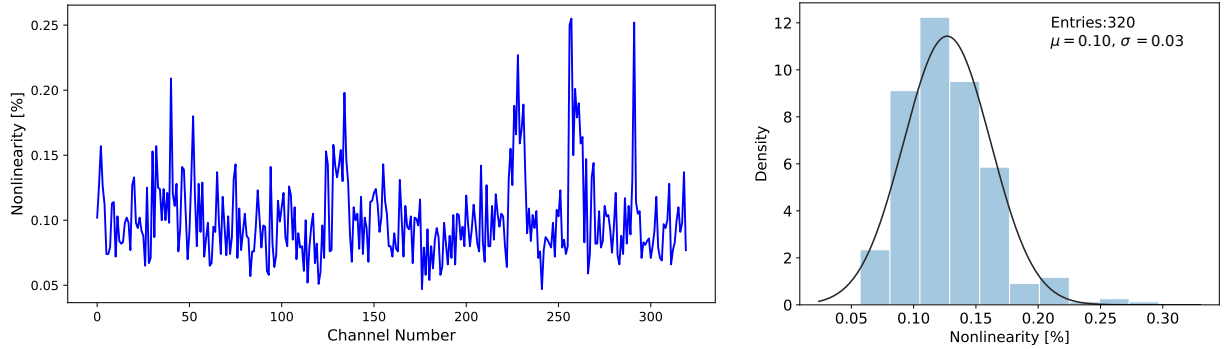


Figure 33: Example INL distribution of an EMB LTDB. The left plot shows the INL of each channel, and the right histogram shows the distribution of the INL values of all the 320 channels with an overlaid Gaussian fit. The average INL is 0.10%.

5.3 Full chain tests

The full chain of the LAr trigger and data acquisition electronics including the Front-End and the Back-End electronics is tested in situ after installing the parts of the Phase-I upgrade electronics in the ATLAS cavern. A set of input signal scans is designed to validate the new system: mapping scans to check the connectivity of all channels; timing scans to align various components in time; and calibration scans to validate the pedestal values, the shape of the pulse and the value and linearity of the gains.

Due to the installation of the new baseplanes and the LTDBs, the electronic path for some of the input channels to the legacy trigger towers were modified. Moreover, the FEBs were removed from the old baseplanes, refurbished with new LSBs and installed on the new baseplanes. These operations might have affected the electronic legacy main readout. The legacy trigger system is required to run in parallel to the new digital trigger system during Run 3. For these reasons, both main and trigger legacy readout paths are validated after the installation of the new Front-End electronics. The noise levels for the different cells and Trigger Towers before and after the installation of the new baseplanes and LTDBs can be seen in Figure 34 and 35 respectively. No significant change in the level of the electronic noise is observed due to the installation of the new electronic boards. The jump at $\eta = 0.8$ observed in both figures is due to a change in the barrel calorimeter sampling fraction, that affects the conversion of the signal in μA to a signal in MeV.

The timing of the different Trigger Tower channels is also adjusted on the TBBs to take into account the new signal path due to the new boards. The time difference relative to the middle layer channels in the different layers before and after the LTDB installation and before and after the correction is shown in Figure 36.

To validate the new digital trigger path, data from the LTDB are received, time-aligned and processed on the LATOME boards and then sent to the local monitoring path to be collected by a UDP server running on a dedicated machine. More precisely, a calibration pulse is injected in the Front-End electronics synchronously to a delayed L1A signal. The LTDB data, corresponding to 32 ADC samples, are received at 40 MHz and buffered on the LATOME boards, which send the data to the local monitoring path when the L1A is received. To be able to retrieve the 32 ADC samples that correspond to the injected pulse the LATOME boards are time-aligned. With this procedure the shape of the pulse collected by the LATOME can be verified for different energy regimes, as illustrated for one Super Cell in Figure 37. To obtain this

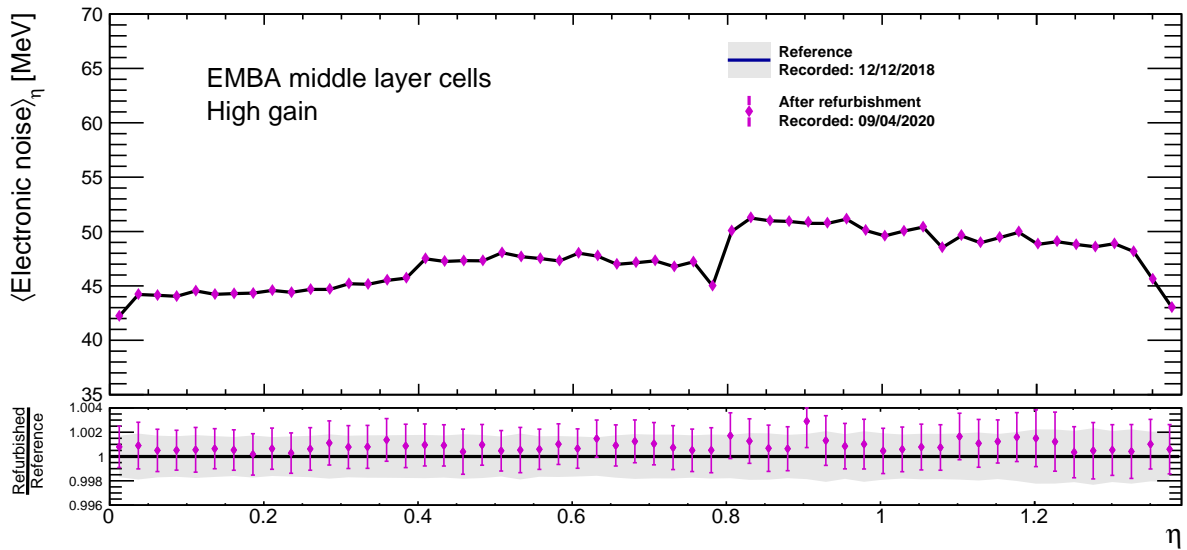


Figure 34: Noise level as function of the pseudorapidity for cells before and after the installation of the new Front-End electronics. The noise level corresponds to the mean value of the readout electronic noise in MeV over the cells in a given pseudorapidity (η) range. Only the cells of the middle layer of the EMB on side A are included. The black line and the gray uncertainty band show the values measured at the end of Run 2. The purple dots show the values measured after the refurbishment of the FECs and FEBs during the LS2. The displayed uncertainties are computed as $\sigma_{\text{noise, cells}}/\sqrt{N_{\text{cells}}}$, where $\sigma_{\text{noise, cells}}$ are the noise values integrated over the cells in the given η range and N_{cells} is the number of cells in the given η range. The cause of the systematic increase of approximately one per mil over the whole η range is under investigation but will have negligible impact on data analyses.

shape with a fine granularity from a 32 ADC sample readout, a series of twenty consecutive calibration pulses is used, each one with an incremental delay of about 1.04 ns. Distortion in the pulse shape can be seen at high energy due to saturation effects which will be discussed in the following.

In order to compute the Super Cell energy from a pulse, the pedestal value must be measured beforehand. Pedestal data are collected without injecting any pulse in the Front-End electronics. From this data, the electronic noise can also be studied since it corresponds to the root mean square of the pedestal value. In Figure 38 the pedestal value and its root mean square can be seen as function of the η position of the Super Cells, in the EMB and EMEC areas and for the different calorimeter layers. They are found to be consistent with the expectation from the design of the LTDB boards, with the electronic noise always smaller than 1 ADC count.

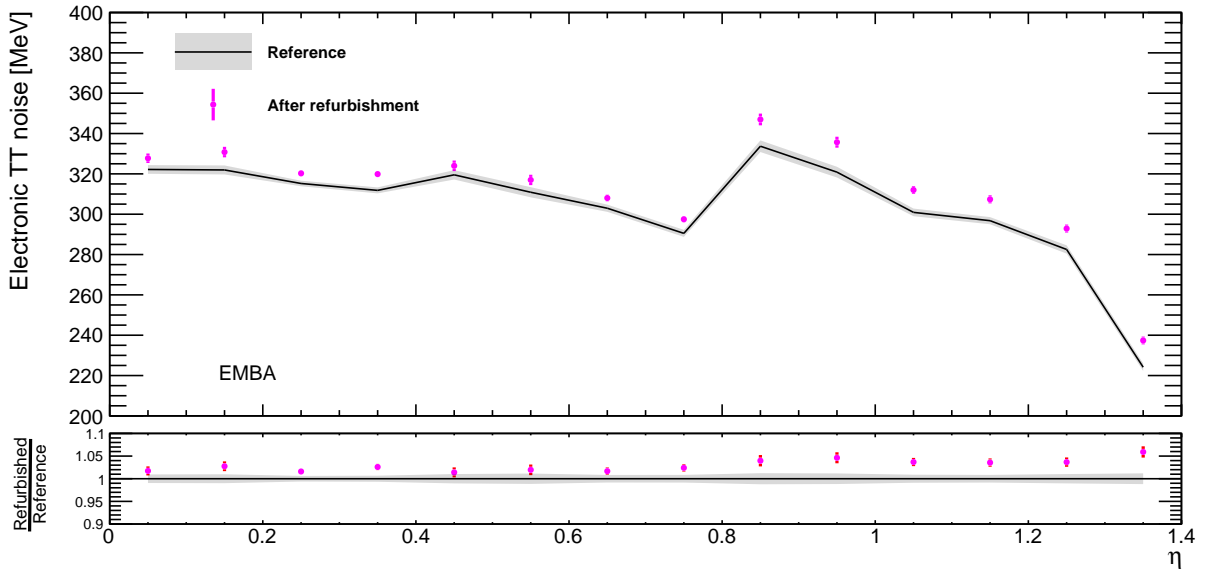


Figure 35: Noise level as function of the pseudorapidity for Trigger Towers (TTs) before and after the installation of the new trigger readout electronics. The noise level corresponds to the mean value of the readout electronic noise in MeV over the TTs in the same pseudorapidity (η) position. Only the TTs of the EMB on side A are included. The black line and the gray uncertainty band show the values measured at the end of Run 2. The purple dots show the values measured after the refurbishment of the FECs and FEBs and the installation of the LTDBs during the LS2. The displayed uncertainties are computed as $\sigma_{\text{noise, TT}}/\sqrt{N_{\text{TT}}}$, where $\sigma_{\text{noise, TT}}$ are the noise values integrated over the TTs in the given η position and N_{TT} is the number of TTs in the given η position. The systematic increase of approximately 2 to 5% over the whole η range is due to a more complex analog signal path and has a negligible impact on trigger performance.

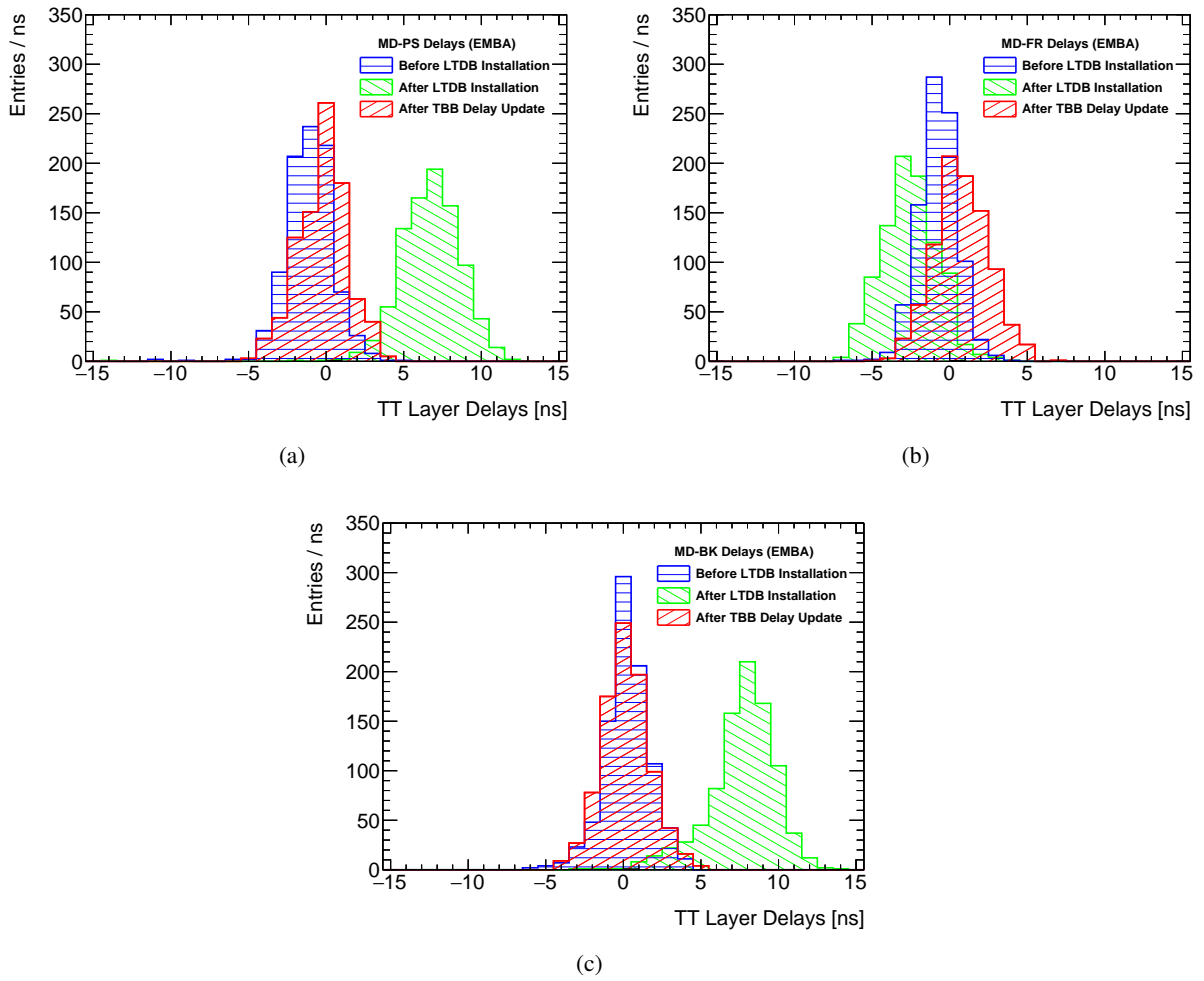


Figure 36: Time difference between (a) middle (MD) layer and presampler (PS) channels, (b) between middle and front (FR) layer channels, and (c) between middle and back (BK) layer channels before and after the baseplane replacement and the LTDB insertion. After the corrections applied to the TBB delays to take into account the new hardware, the distributions match well. Only EMB side A is considered here.

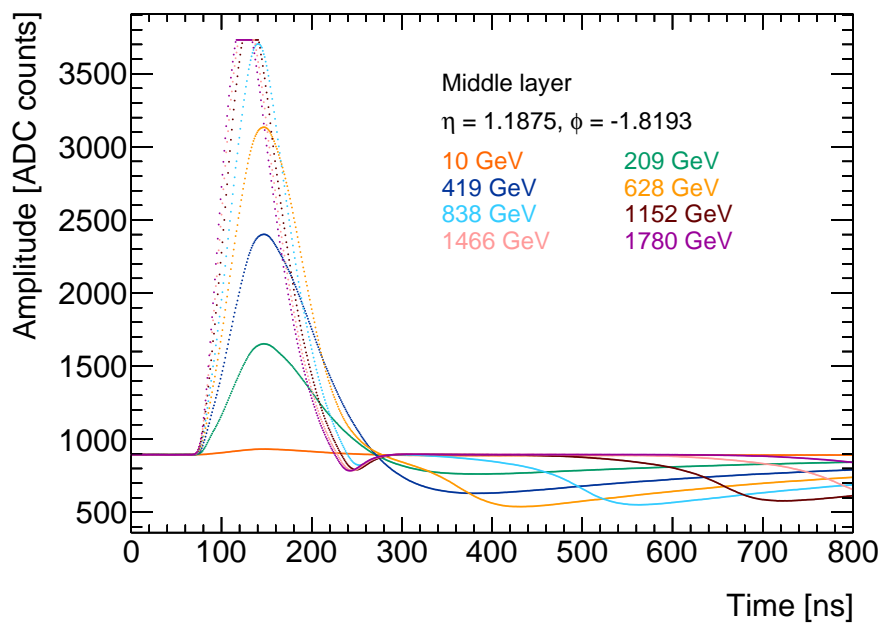


Figure 37: Pulse shape collected by the LATOME board for one Super Cell in the barrel part of the detector at $\eta = 1.1875$ and $\phi = -1.8193$ in the middle layer for several injected current pulses corresponding to different E_T values.

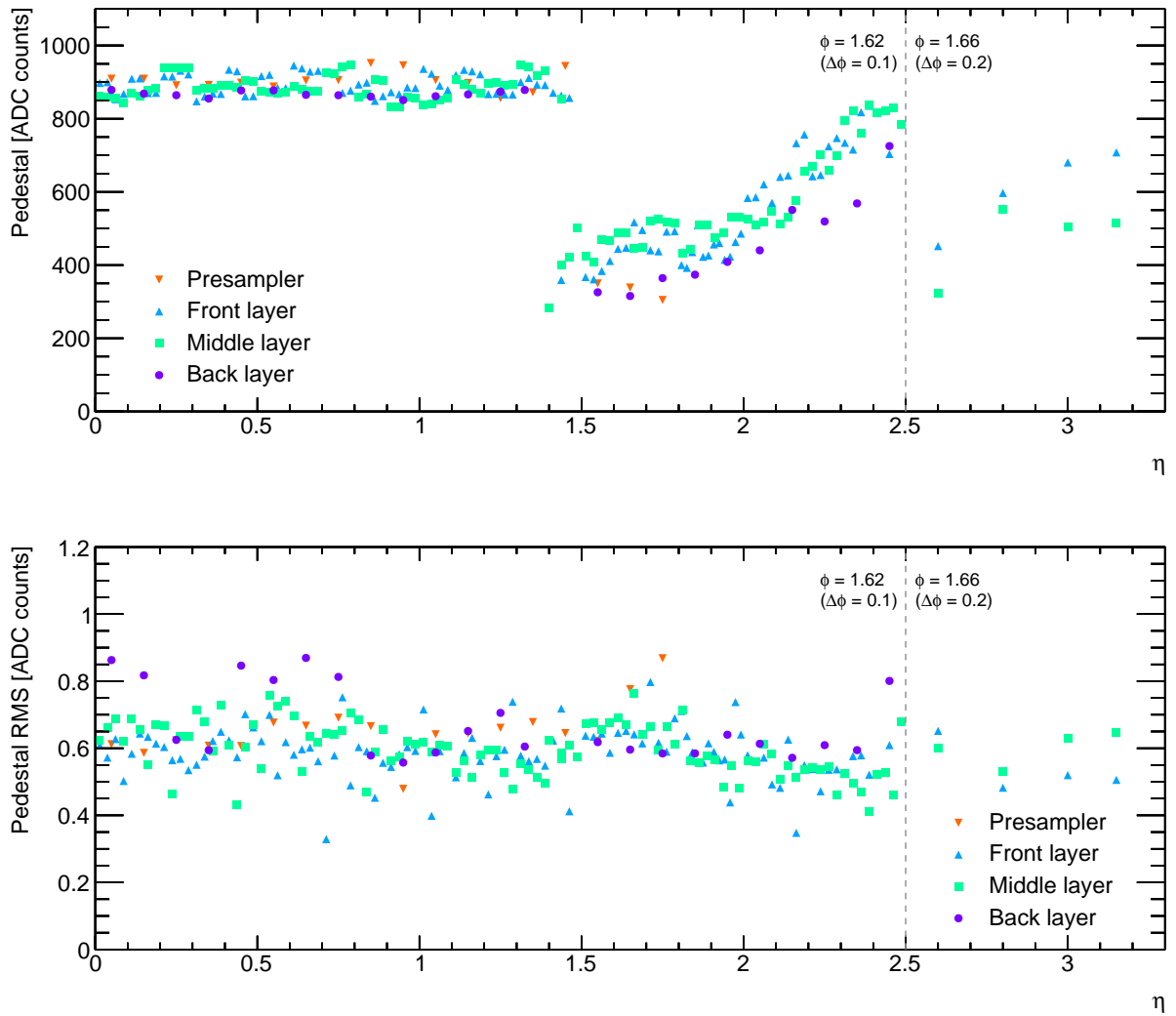


Figure 38: The pedestal value (top) and its root mean square (bottom) as function of the η position of the Super Cells at $\phi = 1.62$ ($\phi = 1.66$) and $0 < \eta < 2.5$ ($2.5 < \eta < 3.2$), corresponding to a $\Delta\phi$ granularity of 0.1 (0.2) and for the different calorimeter layers.

The linearity of the new digital trigger chain is measured using a ramp run similar to the one described in Section 5.1. The peak ADC value with respect to the pedestal as function of the E_T corresponding to the injected pulse as seen by four channels on a LATOME board is presented in Figure 39. The peak ADC value is extracted with an optimal filtering algorithm [41]. The ADC values are linearly increasing with the deposited E_T up to about 800 GeV, where saturation of the Super Cell pulse occurs. This saturation is mainly due to the analog electronics (Linear Mixer), however digital saturation can occur for some channels in addition to the analog one at very high energies.

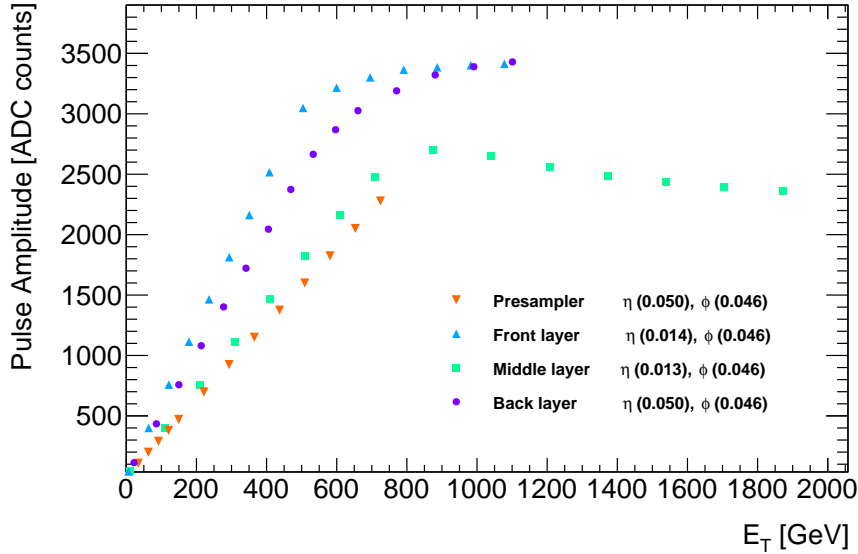


Figure 39: Peak ADC value with respect to the pedestal as function of the E_T corresponding to the injected pulse as seen on a LATOME board by four channels of the different calorimeter layers.

The E_T per ADC count is computed from the ramp runs. This value is shown in Figure 40 as function of the pseudorapidity in the EMB and EMEC areas. The jump at $\eta = 0.8$ is due to a change in the EMB sampling fraction, the one at $\eta = 1.5$ corresponds to the EMB-EMEC transition and the one at $\eta = 2.5$ to the boundary between the EMEC inner and outer wheels. The values are consistent with the ones expected from the design of the LTDB boards.

The main readout system, which reads individual cells of the LAr calorimeter, is well understood and calibrated based on years of ATLAS operation. To fully validate the trigger system, the E_T values computed by the LATOME for certain Super Cells are compared to the sum of E_T values computed for the corresponding cells using data collected with the main readout. The data are collected simultaneously by both readout paths after injecting an electronic pulse in the Front-End electronics. In both cases the E_T values are computed with an optimal filtering algorithm [41]. Figure 41 shows good agreement between the Super Cell E_T and the sum of the E_T values in the corresponding cells for the middle layer of the calorimeter in the barrel region. At high energy the Super Cell pulse shape is saturated and the energy computed using the LATOME data does not increase anymore with the deposited energy.

A similar comparison is performed between the Trigger Tower E_T computed by the legacy trigger system and the sum of the E_T values in the corresponding cells. Figure 41 shows good agreement between the two E_T measurements, with a saturation that occurs earlier in energy than with the Super Cell readout.

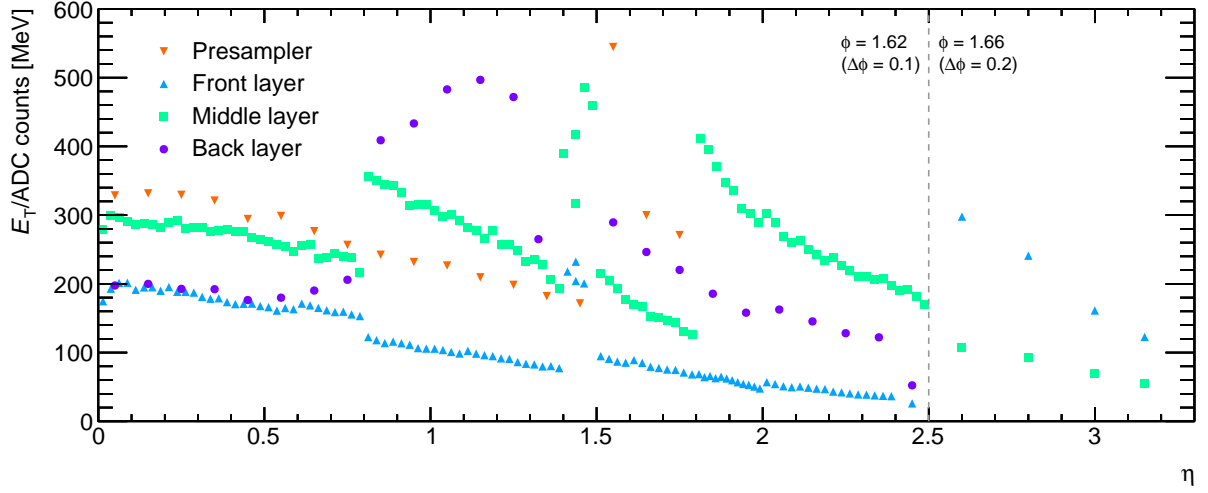


Figure 40: Measured E_T per ADC count as function of the η position of the Super Cells at $\phi = 1.62$ ($\phi = 1.66$) and $0 < \eta < 2.5$ ($2.5 < \eta < 3.2$), corresponding to a $\Delta\phi$ granularity of 0.1 (0.2) and for the different calorimeter layers.

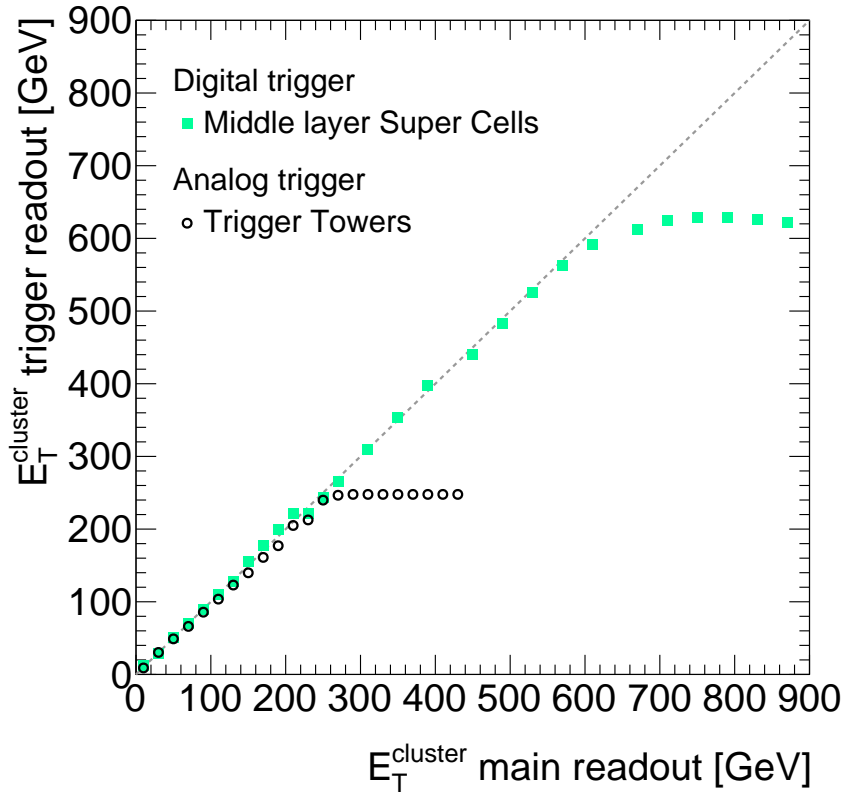


Figure 41: Comparison between the E_T deposited in middle layer Super Cells or Trigger Towers and the sum of the E_T in the corresponding cells of the LAr barrel calorimeter. The Super Cell data are collected by the LATOME boards while the energy deposited in the cells and the Trigger Towers is collected by the legacy main and trigger readout systems for injected signals. The deposited energy measured by the LATOME or the legacy trigger system corresponds well to the one measured by the main readout system up to the level where the signal on the Super Cells or the legacy Trigger Towers is saturated.

5.4 System latency

As discussed in the introduction, the scope of the ATLAS Phase-I upgrades is limited to a few subdetectors. The readout of most of the systems remains unchanged, limiting the capability of extending some of the parameters of the Level-1 trigger system, such as the maximum rate and maximum latency. This situation will only change with the Phase-II upgrades. ATLAS maintains a precise bookkeeping, for each subdetector contributing to the Level-1 trigger, of the different elements leading to the latency of the ATLAS L1A decision. Table 6 details the measured latency for the LAr trigger path starting from the proton-proton collision time up to the reception of the computed energy by the FEX system. The total latency amounts to 43.8 BCs (one BC corresponds to a 25 ns time interval). The listed numbers account for the slowest path; the detector readout being heterogeneous not all signals have the same latency (e.g. due to optical fiber cables of different lengths) although they are all aligned at the input of the LATOME firmware. At its output, corresponding to the encoding and summing firmware block in Table 6, the listed latency is the one of the data sent to the jFEX system. The data sent to eFEX and gFEX systems have a lower latency by 0.4 and 0.1 BCs, respectively. The results in Table 6 are consistent with the measurements of the single ASIC components [43] of the LTDB and with the simulations and on-target measurements of the firmware code operating in a standalone setup.

In addition to the LAr part, the FEX processors require 14 BCs [1] to extract the trigger primitives and transmit them to the Topological Trigger processors. The overall 57.8 BCs latency of the calorimeter trigger system conforms with the maximum (65 BCs) value allowed by ATLAS at the input of the Topological Trigger processors where data from both the calorimeter and the muon trigger modules are combined.

Table 6: Latency measurements for the Phase-I upgrade of the LAr trigger readout electronics. BCs correspond to 25 ns time intervals.

	Latency		Sub-total [BCs]	Total [BCs]
	[ns]	[BCs]		
Time-of-flight at $\eta = 2$	15.0	0.6		
Cable to pulse preamplifier	30.0	1.2		
Preamplifier, shaper, and linear mixer	21.6	0.9	2.7	2.7
LTDB	153.7	6.1	6.1	8.8
Optical fiber cable (77 m) LTDB to LDPB	385.0	15.4	15.4	24.2
Deserializing and descrambling	81.1	3.2		
BCID aligning	28.2	1.1		
Channel remapping	67.7	2.7		
Optimal filtering	108.2	4.3		
Encoding and summing	94.6	3.8		
Serializing	35.7	1.4	16.6	40.8
Optical fiber cable (15 m) LDPB to FEX	75.0	3.0	3.0	43.8

6 Conclusion

The ATLAS Liquid Argon Calorimeter Phase-I upgrade of its trigger readout electronics increases the readout granularity by up to a factor of ten, enabling shower shape parameter calculation at the Level-1 trigger stage and thereby increasing the trigger rejection power while retaining high efficiency. The upgrade provides substantial improvement to the Level-1 trigger electron, photon, jet and missing energy resolution. To realize this trigger system upgrade, new electronic boards including dedicated ASICs were produced and tested to meet specifications and finally installed in the experiment during the second long shutdown of the LHC.

The new trigger readout is being commissioned, and initial tests show that the system is operating according to specifications. The legacy analog trigger readout is kept operational in parallel, reaching the same performance as in Runs 1 and 2 in terms of noise and gain stability without any loss of channels. Noise level, linearity, radiation tolerance and overall energy measurements of the new digital trigger readout meet all expectations.

The next step in the commissioning of the new trigger readout is its full integration with the new ATLAS Level-1 calorimeter trigger system.

Acknowledgements

We thank the support staff from our institutions without whom ATLAS could not be operated efficiently.

We acknowledge the support of CNPq and FAPESP, Brazil; NSERC, NRC, CFI and CMC Microsystems, Canada; CERN; CAS, MOST and NSFC, China; IN2P3-CNRS and CEA-DRF/IRFU, France; BMBF, HGF and MPG, Germany; INFN, Italy; MEXT and JSPS, Japan; MES of Russia, NRC KI, MSHE, Russian Federation; JINR; MSSR, Slovakia; STFC, United Kingdom; DOE and NSF, United States of America. In addition, individual groups and members have received support from Compute Canada and CRC, Canada; ERC, ERDF, Horizon 2020, Marie Skłodowska-Curie Actions and COST, European Union; Investissements d’Avenir Labex, Investissements d’Avenir Idex and ANR, France; DFG and AvH Foundation, Germany; The Royal Society and Leverhulme Trust, United Kingdom.

The crucial computing support from all WLCG partners is acknowledged gratefully, in particular from CERN, the ATLAS Tier-1 facilities at TRIUMF (Canada), NDGF (Denmark, Norway, Sweden), CC-IN2P3 (France), KIT/GridKA (Germany), INFN-CNAF (Italy), NL-T1 (Netherlands), PIC (Spain), ASGC (Taiwan), RAL (UK) and BNL (USA), the Tier-2 facilities worldwide and large non-WLCG resource providers. Major contributors of computing resources are listed in Ref. [44].

We acknowledge, in addition, the excellent work done by employees of the Etablissements Publics pour l’Integration (EPI), Geneva, with the refurbishment of the Front End Boards at the CERN site.

References

- [1] M. Aleksa et al., *ATLAS Liquid Argon Calorimeter Phase-I Upgrade Technical Design Report*, tech. rep. CERN-LHCC-2013-017. ATLAS-TDR-022, CERN, 2013, URL: <https://cds.cern.ch/record/1602230>.

- [2] ATLAS Collaboration, *Performance of the ATLAS Trigger System in 2010*, *Eur. Phys. J. C* **72** (2012) 1849, arXiv: 1110.1530 [hep-ex].
- [3] ATLAS Collaboration, *Luminosity determination in pp collisions at $\sqrt{s} = 13$ TeV using the ATLAS detector at the LHC*, ATLAS-CONF-2019-021, 2019, URL: <https://cds.cern.ch/record/2677054>.
- [4] M. Aharrouche et al., *Energy linearity and resolution of the ATLAS electromagnetic barrel calorimeter in an electron test-beam*, *Nucl. Instrum. Meth. A* **568** (2006) 601, arXiv: [physics/0608012](https://arxiv.org/abs/physics/0608012).
- [5] M. Aharrouche et al., *Response Uniformity of the ATLAS Liquid Argon Electromagnetic Calorimeter*, *Nucl. Instrum. Meth. A* **582** (2007) 429, arXiv: 0709.1094 [physics.ins-det].
- [6] ATLAS Collaboration, *Electron and photon energy calibration with the ATLAS detector using 2015–2016 LHC proton–proton collision data*, *JINST* **14** (2019) P03017, arXiv: 1812.03848 [hep-ex].
- [7] H. Abreu et al., *Performance of the electronic readout of the ATLAS liquid argon calorimeters*, *JINST* **5** (2010) P09003.
- [8] F. Hubaut, B. Laforge, O. Le Dortz, D. Martin and P. Schwemling, *Implementation of a serial protocol for the liquid argon calorimeters of the ATLAS detector*, *IEEE Transactions on Nuclear Science* **48** (2001) 1254, URL: <http://dx.doi.org/10.1109/23.958761>.
- [9] B. G. Taylor, *TTC distribution for LHC detectors*, *IEEE Transactions on Nuclear Science* **45** (1998) 821.
- [10] ATLAS Collaboration, *ATLAS TDAQ System Phase-I Upgrade: Technical Design Report*, ATLAS-TDR-023; CERN-LHCC-2013-018, 2013, URL: <https://cds.cern.ch/record/1602235>.
- [11] J. Anderson et al., *FELIX: a PCIe based high-throughput approach for interfacing front-end and trigger electronics in the ATLAS Upgrade framework*, *JINST* **11** (2016) C12023.
- [12] P. Moreira, A. Marchioro and Kloukinas, *The GBT: A proposed architecture for multi-Gb/s data transmission in high energy physics*, *Proceedings, Topical Workshop on Electronics for Particle Physics (TWEPP07)* (2007) 332.
- [13] P. Moreira et al., *The GBT Project*, *Proceedings, Topical Workshop on Electronics for Particle Physics (TWEPP09)* (2009) 342.
- [14] A. Barriuso Poy et al., *The detector control system of the ATLAS experiment*, *JINST* **3** (2008) P05006.
- [15] D. Axen et al., *Signal feedthroughs for the ATLAS barrel and endcap calorimeters*, *Rev. Sci. Instrum.* **76** (2005) 063306.
- [16] N. J. Buchanan et al., *Design and implementation of the Front End Board for the readout of the ATLAS liquid argon calorimeters*, *JINST* **3** (2008) P03004.
- [17] N. J. Buchanan et al., *Radiation qualification of the front-end electronics for the readout of the ATLAS liquid argon calorimeters*, *JINST* **3** (2008) P10005.

- [18] ATLAS Collaboration, *Technical Design Report for the Phase-II Upgrade of the ATLAS LAr calorimeter*, tech. rep. CERN-LHCC-2017-018. ATLAS-TDR-027, CERN, 2017, URL: <https://cds.cern.ch/record/2285582>.
- [19] J. Kuppambatti et al., *A radiation-hard dual-channel 12-bit 40 MS/s ADC prototype for the ATLAS Liquid Argon calorimeter readout electronics upgrade at the CERN LHC*, *Nucl. Instrum. Meth. A* **855** (2017) 38, arXiv: 1706.01535 [physics.ins-det].
- [20] T. Andeen et al., *Performance and Quality Control of a Radiation-Hard 12-bit 40 MSPS ADC for the ATLAS Liquid Argon Calorimeter Trigger Readout Electronics Phase-I Upgrade at the LHC*, *JINST* **15** (2020) P04012, arXiv: 1912.06093 [physics.ins-det].
- [21] J. Kuppambatti, J. Ban, T. Andeen, P. Kinget and G. Brooijmans, *A radiation-hard dual channel 4-bit pipeline for a 12-bit 40 MS/s ADC prototype with extended dynamic range for the ATLAS Liquid Argon Calorimeter readout electronics upgrade at the CERN LHC*, *JINST* **8** (2013) P09008, arXiv: 1308.0028 [physics.ins-det].
- [22] L. Xiao et al., *LOCx2, a low-latency, low-overhead, 2 × 5.12-Gbps transmitter ASIC for the ATLAS Liquid Argon Calorimeter trigger upgrade*, *JINST* **11** (2016) C02013, arXiv: 2009.08627 [physics.ins-det].
- [23] P. Moreira et al., *The GBT-SerDes ASIC prototype*, *JINST* **5** (2010) C11022.
- [24] X. Zhao et al., *Mid-board miniature dual channel optical transmitter MTx and transceiver MTRx*, *JINST* **11** (2016) C03054, arXiv: 2009.08623 [physics.ins-det].
- [25] X. Li et al., *8-Gbps-per-channel radiation-tolerant VCSEL drivers for the LHC detector upgrade*, *JINST* **10** (2015) C02017.
- [26] M. Menouni, P. Gui and P. Moreira, *The GBTIA, a 5 Gbit/s Radiation-Hard Optical Receiver for the SLHC Upgrades*, *Proceedings, Topical Workshop on Electronics for Particle Physics (TWEPP09)* (2009) 326.
- [27] P. Farthouat and H. Williams, *ATLAS policy on radiation tolerant electronics*, (1997), URL: <http://cdsweb.cern.ch/record/683666/>.
- [28] Versatile Link, *Versatile Link Project Public Area*, <https://espace.cern.ch/project-versatile-link/public/default.aspx>, Accessed: 2022-05-04, 2014.
- [29] L. Xiao et al., *A low-latency, low-overhead encoder for data transmission in the ATLAS Liquid Argon Calorimeter trigger upgrade*, *Nucl. Instrum. Meth. A* **831** (2016) 288.
- [30] A. Caratelli et al., *The GBT-SCA, a radiation tolerant ASIC for detector control and monitoring applications in HEP experiments*, *JINST* **10** (2015) C03034.
- [31] S. Bonacini, K. Kloukinas and P. Moreira, *E-link: A Radiation-Hard Low-Power Electrical Link for Chip-to-Chip Communication*, *Proceedings, Topical Workshop on Electronics for Particle Physics (TWEPP09)* (2009) 422.
- [32] N. Boetti, P. Jarron, B. Kisielewski and F. Faccio, *Radiation performance of the L4913 voltage regulator*, *IEEE Radiation Effects Data Workshop, Phoenix, AZ, USA, 2002*, pp. 115-119 (2002).

- [33] S. Fiore et al., *Radiation and magnetic field effects on commercial DC-DC converters for HL-LHC experiments*, IEEE Nuclear Science Symposium and Medical Imaging Conference (NSS/MIC), Seattle, WA, USA, 2014, pp. 1-3 (2014).
- [34] J. Ameel et al., *Radiation-hard power electronics for the ATLAS New Small Wheel*, JINST **10** (2015) C01009.
- [35] M. Lazzaroni, M. Citterio, S. Latorre, A. Lanza and G. Spiazzi, *Testing the behavior in hostile environment of Points of Load for LHC experiments*, Measurement **75** (2005) 161.
- [36] ATLAS Collaboration, *Technical Design Report for the Phase-II Upgrade of the ATLAS TDAQ System*, tech. rep. CERN-LHCC-2017-020. ATLAS-TDR-029, CERN, 2017, URL: <https://cds.cern.ch/record/2285584>.
- [37] F. Bellachia, *ICARE - Intelligent platform management Controller software*, URL: <https://gitlab.cern.ch/atlas-lar-icare/ICARE>.
- [38] C. Ghabrous Larrea et al., *IPbus: a flexible Ethernet-based control system for xTCA hardware*, JINST **10** (2015) C02019.
- [39] Intel, *Avalon Interface specification v20.1*, tech. rep. MNL-AVABUSREF, Intel, 2020, URL: https://www.intel.com/content/dam/www/programmable/us/en/pdfs/literature/manual/mnl_avalon_spec.pdf.
- [40] B. Deng et al., *A line code with quick-resynchronization capability and low latency for the optical data links of LHC experiments*, JINST **9** (2014) P07020.
- [41] W. E. Cleland and E. G. Stern, *Signal processing considerations for liquid ionization calorimeters in a high rate environment*, Nucl. Instrum. Meth. A **338** (1994) 467.
- [42] D. Besin et al., *Design and Evaluation of the LAr Trigger Digitizer Board in the ATLAS Phase-I Upgrade*, IEEE Transactions on Nuclear Science **66** (2019) 2011.
- [43] B. Deng et al., *The latency validation of the optical link for the ATLAS Liquid Argon Calorimeter Phase-I trigger upgrade*, JINST **13** (2018) P05002, arXiv: [2009.06143](https://arxiv.org/abs/2009.06143) [physics.ins-det].
- [44] ATLAS Collaboration, *ATLAS Computing Acknowledgements*, ATL-SOFT-PUB-2021-003, URL: <https://cds.cern.ch/record/2776662>.